

OH Evolution in Molecular Clouds

NINGYU TANG,¹ DI LI,^{1,2,3} NANNAN YUE,^{1,2} PEI ZUO,^{4,5,2} TIE LIU,^{6,7} GAN LUO,^{1,2} LONGFEI CHEN,¹ SHENG-LI QIN,⁸
YUEFANG WU,^{9,10} AND CARL HEILES¹¹

¹CAS Key Laboratory of FAST, National Astronomical Observatories, Chinese Academy of Sciences, Beijing 100101, People's Republic of China

²University of Chinese Academy of Sciences, Beijing 100049, People's Republic of China

³NAOC-UKZN Computational Astrophysics Centre, University of KwaZulu-Natal, Durban 4000, South Africa

⁴Kaoli Institute for Astronomy and Astrophysics, Peking University, Beijing 100871, China

⁵International Centre for Radio Astronomy Research (ICRAR), The University of Western Australia, 35 Stirling Hwy, Crawley, WA 6009, Australia

⁶Shanghai Astronomical Observatory, Chinese Academy of Sciences, 80 Nandan Road, Shanghai 200030, People's Republic of China

⁷Key Laboratory for Research in Galaxies and Cosmology, Chinese Academy of Sciences, 80 Nandan Road, Shanghai 200030, People's Republic of China

⁸Department of Astronomy, Yunnan University, Kunming 650091, China

⁹Department of Astronomy, School of Physics, Peking University, 100871 Beijing, China

¹⁰Kavli Institute for Astronomy and Astrophysics, Peking University, 100871 Beijing, China

¹¹Department of Astronomy, University of California, Berkeley, 601 Campbell Hall 3411, Berkeley, CA 94720-3411, USA

ABSTRACT

We have conducted OH 18 cm survey toward 141 molecular clouds in various environments, including 33 optical dark clouds, 98 Planck Galactic cold clumps (PGCCs) and 10 Spitzer dark clouds with the Arecibo telescope. The deviations from local thermal equilibrium are common for intensity ratios of both OH main lines and satellite lines. Line intensity of OH 1667 MHz is found to correlate linearly with visual extinction A_V when A_V is less than 3 mag. It was converted into OH column density by adopting excitation temperature derived from Monte Carlo simulations with one sigma uncertainty. The relationship between OH abundance $X(\text{OH})$ relative to H_2 and A_V is found to follow an empirical formula,

$$\frac{X(\text{OH})}{10^{-7}} = 1.3_{-0.4}^{+0.4} + 6.3_{-0.5}^{+0.5} \times \exp\left(-\frac{A_V}{2.9_{-0.6}^{+0.6}}\right).$$

Linear correlation is found between OH and ^{13}CO intensity. Besides, nonthermal velocity dispersions of OH and ^{13}CO are closely correlated. These results imply tight chemical evolution and spatial occupation between OH and ^{13}CO . No obvious correlation is found between column density and nonthermal velocity dispersion of OH and HI Narrow Self-Absorption (HINSA), indicating different chemical evolution and spatial volume occupation between OH and HINSA. Using the age information of HINSA analysis, OH abundance $X(\text{OH})$ is found to increase linearly with cloud age, which is consistent with previous simulations. Fourteen OH components without corresponding CO emission were detected, implying the effectiveness of OH in tracing the ‘CO-dark’ molecular gas.

Keywords: ISM: clouds — ISM: evolution — ISM: molecules.

1. INTRODUCTION

The hydroxyl radical (OH) transition was firstly detected at 18 cm band in the interstellar medium (ISM) in 1963 (Weinreb et al. 1963). It was

found to exist in various environments, for instance, dark molecular clouds (e.g., Heiles 1969; Crutcher 1973), diffuse/translucent molecular clouds (e.g., Grossmann et al. 1990; Barriault et al. 2010; Cotten et al. 2012; Dawson et al. 2014), and the regions without CO emission while OH is detected in emission (e.g., Allen et al. 2012, 2015; Busch et al. 2019) or ab-

sorption toward continuum sources (e.g., Li et al. 2018; Rugel et al. 2018).

There are four hyperfine transitions (1612.231, 1665.402, 1667.359 and 1720.530 MHz) of $^2\Pi_{3/2}$ $J=3/2$ ground state of OH (Fig. 1). The line strengths of these four transitions are considered to follow $T_A^{1612}:T_A^{1665}:T_A^{1667}:T_A^{1720}=1:5:9:1$ under the local thermodynamic equilibrium (LTE). It was found that the observed line strengths ratio always deviate from the intrinsic 1:5:9:1 ratio due to the effect of surrounding environment. In most cases, the 1612 and 1720 MHz satellite lines appear as ‘conjugate’ behavior (with one transition being in emission and the other one being in absorption) and ‘flip’ behavior (with transition from emission to absorption in 1612 or 1720 transition alone), which may originate from the infrared pumping by its surrounding source (e.g., Crutcher 1977). Due to sensitive dependence on radiation field, the OH satellite lines are ideal indicator of external illumination environment of the clouds. The excitation of main lines (1665 and 1667 MHz) should be less affected because the quantum number F values of upper and lower population levels are same. However, OH absorptions toward continuum sources indicate that the non-thermal excitation are common for main lines (e.g., Dickey et al. 1981; Li et al. 2018).

OH abundance relative to H_2 is a critical parameter for studying OH evolution of ISM. Previous observations suggested a commensal value of 1×10^{-7} toward nearby interstellar medium (ISM) (e.g., Sancisi et al. 1974; Turner & Heiles 1974; Crutcher & Watson 1976). Nguyen et al. (2018) found a consistent result by explicit OH absorption observations against continuum sources. Most of the OH abundance measurements were made toward the positions with visual extinction $A_V \leq 5$ mag.

Previous OH observations focus on nearby giant molecular clouds, e.g., Ophiuchus cloud (Myers et al. 1978; Ebisawa et al. 2015) or diffuse region of translucent clouds (Cotten et al. 2012). In order to systematically investigate OH evolution in molecular clouds in various environments, we conducted OH survey toward molecular clouds with different environments, which includes optical dark clouds, Spitzer 8 μm dark clouds and Planck cold clumps. With a density range of 10^2 to 10^5 cm^{-3} , visual extinction range of 1 to 60 mag and scale size from 0.1 pc to tens of pc, these clouds are undergoing different evolution stages, from star-less quiet state to cluster star formation (Meng et al. 2013; Zhang et al. 2016; Negrello et al. 2017). The observations would provide us a full view of the OH evolution in molecular clouds.

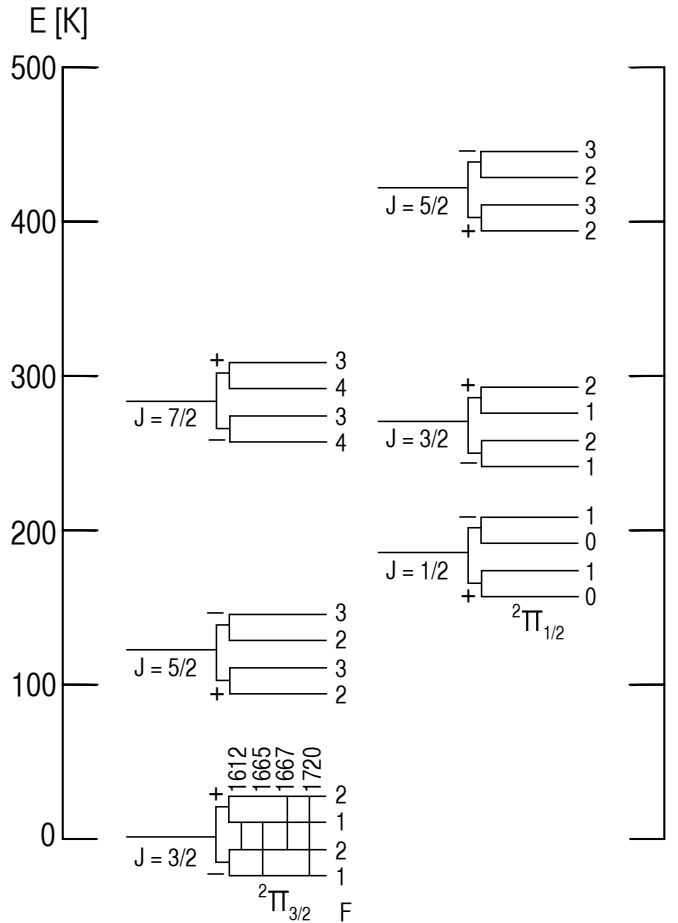


Figure 1. Energy level diagram of OH $^2\Pi_{3/2}$ and $^2\Pi_{1/2}$ states (Ebisawa et al. 2015). J and F represent total angular momentum quantum number without and with the nuclear spin, respectively. ‘+’ and ‘-’ represent the Λ -type doubling levels. A transition between two energy levels is allowed when the energy levels have different Λ -types and satisfy the $\Delta J = 0, \pm 1$ and $\Delta F = 0, \pm 1$ condition. The OH 1612, 1665, 1667 and 1720 MHz transitions happen between hyperfine levels of the $^2\Pi_{3/2}$ ($J=3/2$).

This paper is organized as follows. In section 2, we describe the details of observations and data. In section 3, the observation results of OH are described. OH abundance and the relationships between OH and other molecular tracers are investigated in section 4 and 5. Discussion and summary are presented in section 6 and section 7, respectively.

2. OBSERVATIONS AND ARCHIVAL DATA

2.1. Source Selection

The optical dark clouds (ODCs) are selected based on the catalog of Dutra & Bica (2002). Those ODCs with angular diameter that is larger than the beam width of Arecibo telescope (~ 3.1 arcmin at 1.6 GHz) were

selected. Finally, data were observed toward 33 ODCs, including 21 sources in the first quarter and 12 sources in the anti-center direction. The visual extinction of 29 ODCs ranges from 1 to 5 mag, while visual extinction of 4 sources (LDN621, LDN638, LDN649 and LDN673) exceeds the value of 5 mag.

The Planck Galactic cold clumps (PGCCs) were selected from the catalog of [Planck Collaboration et al. \(2011\)](#). Those clumps having CO emission ([Wu et al. 2012](#)) and the feature of HI self absorption were preferred. A total of 98 PGCCs with visual extinction range of 0.3 to 5 mag were observed. Same as ODCs, PGCCs in both first quarter and anti-center direction were selected.

The 10 Spitzer dark clouds (SDCs) with visual extinction $A_V \geq 5$ mag were selected from the catalog of [Peretto & Fuller \(2009\)](#). All these SDCs were confirmed to have Young Stellar Object (YSO) associated.

The spatial distribution of these sources is shown in Fig. 2. These sources are almost symmetric with Galactic latitude in the first quart of Milky Way and associated with giant molecular clouds (e.g., Taurus) in the anti-center direction. Spectral observations and auxiliary data are described as follows.

2.2. OH Observations with Arecibo Telescope

Observations of the OH 18 cm transitions were carried out with the Arecibo 300-m telescope, whose beam size is 3.5 arcmin at 1.6 GHz. Total-ON mode was adopted during observations since the ripple of spectral bandpass is stable and has a width that is much larger than that of typical Galactic spectral lines (\sim several km s^{-1}). The bandpass after removing windows containing OH lines was subtracted by linear or polynomial fitting. We adopted the Interim Correlator backend with a bandwidth of 3.125 MHz in 8192 channels, leading to a spectral resolution of 0.069 km s^{-1} at 1.66 GHz. The spectra were smoothed by a factor of two, resulting in spectral resolution of 0.138 km s^{-1} . The observation date, backend setting and sensitivity are different for three categories of samples.

ODC: Three transitions of OH, 1612.2310, 1665.4018, and 1667.3590 MHz were obtained during September and October, 2018. Each source was integrated for 20 minutes, leading to a spectral root-mean-square (rms) of $\sim 21 \text{ mK}$ in T_A under velocity resolution of 0.138 km s^{-1} at 1.66 GHz.

PGCC: Four transitions of OH, 1612.2310, 1665.4018, 1667.3590 and 1720.5300 MHz were obtained between November 2013 and November 2015. Total integration time is 5 minutes for each source, resulting in a rms of

$\sim 44 \text{ mK}$ in T_A under velocity resolution of 0.138 km s^{-1} at 1.66 GHz.

SDC: The observations were taken in November 2013 with same setting as that of PGCCs.

A main beam efficiency of 0.5 ([Heiles et al. 2001](#)) was used to convert the spectra from antenna temperature into main-beam brightness temperature.

2.3. Observations of CO Molecular Lines

$^{12}\text{CO}(1-0)$ and its isotopes ($^{13}\text{CO}(1-0)$ and $\text{C}^{18}\text{O}(1-0)$) observations toward 33 ODCs, 11 PGCCs and 10 SDCs were made with Delingha 13.7m during May and June, 2020. The beam width and main-beam efficiency of the telescope are ~ 50 arcsec and ~ 0.51 at 115 GHz. The system temperatures of these observations vary from 230 K to 350 K, with a typical value of 250 K. The backend has a bandwidth of 1 GHz and channel width of 61 kHz, which corresponds a velocity resolution of 0.16 km s^{-1} at 115.271 GHz. Integration time of each source was around 10 minutes to reach a spectral rms of $\sim 0.15 \text{ K}$ (T_{mb}) in 0.16 km s^{-1} .

CO data of rest 87 PGCCs were obtained from CO survey with Delingha 13.7m in 2011 ([Wu et al. 2012](#)). Channel rms of these spectra is $\sim 0.2 \text{ K}$ (T_A) in 0.16 km s^{-1} .

2.4. HI and $N(\text{H}_2)$ Data

HI spectra toward ODCs were obtained simultaneously with OH data, resulting in rms of $\sim 15 \text{ mK}$ (T_A) in 0.15 km s^{-1} . HI data of rest sources were extracted from the Galactic Arecibo L-band Feed Array HI (GALFA-HI; [Peek et al. 2018](#)), with a rms of 0.33 K in 0.18 km s^{-1} .

The total column density of H_2 , $N(\text{H}_2)$ were derived by dust emission. The values of $N(\text{H}_2)$ for PGCCs and SDCs were obtained from [Planck Collaboration et al. \(2016\)](#) and [Peretto et al. \(2016\)](#). For ODCs, we utilized the E(B-V) data from [Schlegel et al. \(1998\)](#) (SFD98). The conversion factor of 3.1 between visual extinction A_V and E(B-V) was adopted ([Schultz & Wiemer 1975](#)). $N(\text{H}_2)$ were derived by eliminating HI contribution along sightline.

3. RESULTS

3.1. OH Thermal Emission

Sample spectra with OH detection toward ODCs, PGCCs and SDCs are shown in Fig. 3. OH main-lines always appear as emission in the ODCs and PGCCs while appear as absorption in SDCs. Strong continuum background (e.g., from H II region) associated with star formation regions may contribute to the absorption feature in SDCs. We identified OH components in velocity by applying Gaussian decomposition. The

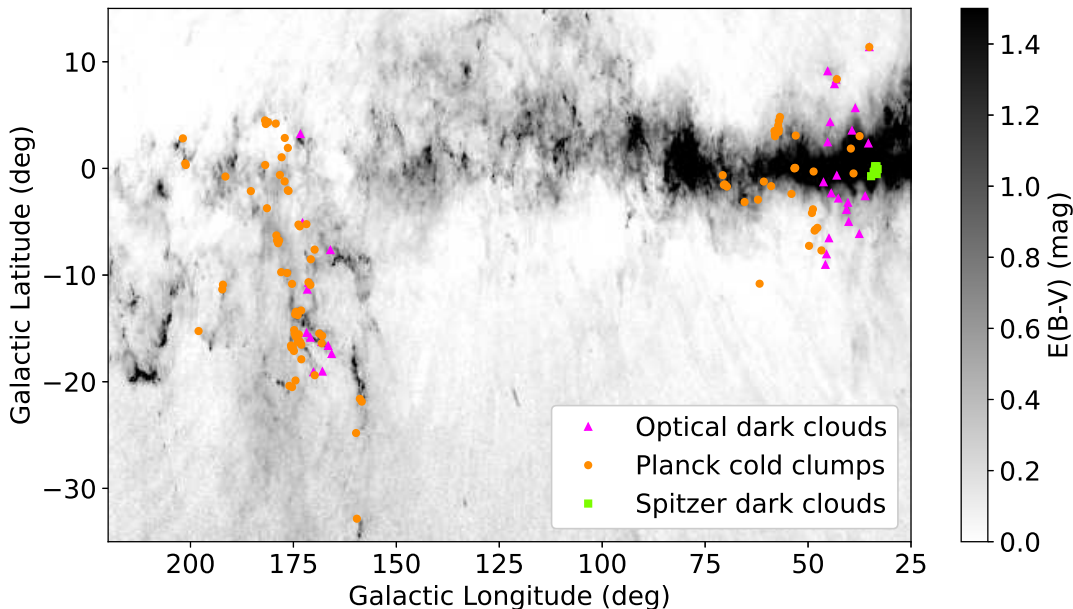


Figure 2. Spatial distribution of sources overlaid on the Planck extinction map. The value of extinction ranges from 0 (white) to 1.5 (black) mag.

results are shown in Table 2. Most sources have only one OH/CO component in velocity. Multiple OH/CO components with close central velocities were detected toward 33% of sources, which are believed to contain several spatially related fragments along the line of sight (Magnani & Siskind 1990).

A total of 193 OH thermal components are detected. Both OH 1665 and 1667 emission were detected in 135 components, while OH 1665 and 1667 emissions were detected in 5 and 41 components alone, respectively. The emission of one transition alone may arise from maser excitation instead of thermal emission. But this is difficult to distinguish since we don't have mapping observations.

The strength ratio between OH main lines ($R = T_b^{1667}/T_b^{1665}$) would lie in the range of [1.0, 1.8] when optical depth is considered under thermal excitation. The strength ratio would deviate this range if non-thermal collision or radiation excitation dominates. It is called the OH main-line anomaly.

Statistical result of 135 OH components with detection of two OH main lines is shown in Figure 4. The percentage of OH main-line anomaly is 35.3%, 20.9%, and 33.3% for ODCs, PGCCs and SDCs, respectively. If the case with 1665 or 1667 detection alone is considered as OH main line anomaly, the percentage of OH main-line anomaly would be 60.7%, 36.8%, and 56.5%

for ODCs, PGCCs and SDCs, respectively. This may indicate that PGCCs are less affected by non-thermal effect or external irradiation compared to ODCs and SDCs.

The satellite anomaly in which the satellite line strengths deviate from the LTE ratio is found to be common. We follow Turner (1973) and define the satellite anomaly in the following two types:

- II(a) Overpopulation of the F=1 level of $^2\Pi_{3/2}$ ground state. There are three observational cases for this type: 1) Enhanced 1612 MHz emission and weaker even non-detected 1720 MHz emission when main lines exhibit as emission; 2) Non-detection of 1612 MHz line but there is obvious absorption feature for both 1720 MHz and main-lines; 3) 'Conjugate' behavior of the 1612 emission and 1720 absorption.
- II(b) Overpopulation of the F=2 level of $^2\Pi_{3/2}$ ground state. There are three observational cases for this type: 1) Enhanced 1720 MHz emission and weaker even non-detected 1612 MHz emission when main lines exhibit as emission; 2) Emission or non-detection of 1720 MHz line but there is obvious absorption feature for both 1612 MHz and main-lines; 3) 'Conjugate' behavior of the 1612 absorption and 1720 emission.

Table 1. Statistical number of satellite anomaly types for ODC, PGCC and SDC. The number of sources with associated YSO, IR or FIR target in a radius of 2 arcmin are shown in brackets.

Type	Sub-type	ODC ^a	PGCC	SDC
Π(a)	(1)	2 (1)	8 (2)	0 (0)
Π(a)	(2)	0 (0)	0 (0)	0 (0)
Π(a)	(3)	0 (0)	4 (4)	4 (4)
Π(b)	(1)	1 (0)	30 (13)	0 (0)
Π(b)	(2)	2 (2)	1 (0)	0 (0)
Π(b)	(3)	0 (0)	5 (3)	5 (5)

a: Candidate, since there is no 1720 MHz data for ODCs.

The statistical result of OH satellite anomaly is presented in Table 1. The results for ODC need to be checked further since there is no 1720 MHz observations for ODCs.

Collisional pumping could lead to enhancement of 1720 MHz line but require a relatively high kinetic temperature ($T_K \geq 25$ K) to reach significant population reversion of ground F=1 and F=2 levels (e.g., Turner 1973). The kinetic temperatures of the molecular clouds are around 10 K, which means collisional pumping may contribute little. As seen in Fig. 1, the effect for satellite line anomaly is contributed by far-infrared pumping and decay between the ground level state $^2\Pi_{3/2}$ and higher energy levels of OH (e.g., $^2\Pi_{5/2}$ and $^2\Pi_{1/2}$; Litvak 1969).

As shown in Table 1, Young Stellar Objects(YSO), Infrared sources (IR) or Far-infrared (FIR) targets are found in the vicinity within radius of 2 arcmin toward 34 sources, almost 55% of all sources with OH satellite anomaly. Sixteen of 18 sources with conjugate behavior contain nearby YSOs, IR or FIR objects. This fraction is much higher than the sub-type (1) and (2). This is reasonable since the overpopulation level would increase from sub-type (1) to (3).

Besides, these results imply that nearby sources emitting far-infrared photons are not necessary to lead to satellite anomaly. This is consistent with the conclusion by Harju et al. (2000) that a slightly more intense infrared radiation field than the general Galactic background could lead to OH satellite-line anomaly.

3.2. OH Maser Emission

Three OH stellar maser with strong or multiple emission features were clearly detected toward LDN649, SDC033.107-00.65 and SDC033.332-0.531. They are described in details as follows.

LDN649: As shown in Figure 5(a), this maser has a peak intensity of ~ 0.025 Jy across a velocity range of 10-15 km s⁻¹ in the OH 1665 spectrum. A YSO locates

96 arcsec away from the source position. This maser may arise from the evolved stellar gas of this YSO.

SDC033.107 – 00.65: As shown in Figure 5(b), the maser emission appears in the velocity range of 75-85 km s⁻¹ and has a peak of ~ 2 Jy in the OH 1665 spectrum. It has typical feature of maser associated with high-mass star-forming regions and was reported in the previous OH survey of methanol sources (Szymczak & Gérard 2004). This kind of masers are considered to arise from the the hot cores with high density ($\sim 10^7$ cm⁻³) near ultracompact H II regions.

SDC033.332 – 0.531: In Figure 5(c), this maser exhibits both blue (20 km s⁻¹) and red (60 km s⁻¹) peaks with magnitude of ~ 0.06 Jy, which belongs to typical maser features from an evolved stellar source. No known circumstellar maser was found with 2 arcmin radius of this source. It should be a new detection of circumstellar maser.

4. FURTHER ANALYSIS

4.1. Relation between $W(\text{OH})$ and A_V

The A_V values of ODCs were derived from SFD98, which is believed to trace the total proton along a sightline. It contains two major gas components, HI and H₂, thus $A_V^{\text{LOS}} = A_V(\text{HI}) + A_V(\text{H}_2)$.

To eliminate contribution of A_V value from the HI emission along the sightline of the ODC, we derived HI intensity $I(\text{HI})$ by summing the HI emission T_{mb} from -150 to 150 km s⁻¹ $I(\text{HI}) = \int_{-150}^{150} T_{\text{mb}} dv$. $I(\text{HI})$ was converted to HI column density, $N(\text{HI}) = 1.82 \times 10^{18} I(\text{HI}) / f_{\text{cor}}$ cm⁻², in which f_{cor} represents the correction factor due to HI optical depth τ , $f_{\text{cor}} = \int \tau dv / \int (1 - e^{-\tau}) dv$. Previous absorption observations toward continuum sources show that f_{cor} value of 1-1.8 from HI emission profile (e.g., Dickey & Benson 1982). Due to lack of prior information, we took $f_{\text{cor}} = 1$, which represents optically thin condition and a lower limit of $N(\text{HI})$ for ODCs. The canonical conversion factor between $N(\text{HI})$ and A_V , $A_V(\text{HI}) = N(\text{HI}) / 1.87 \times 10^{21}$ mag was then adopted (Schultz & Wiemer 1975; Bohlin et al. 1978). Uncertainties during this process are discussed in Section 6.4.

Since there exist $N(\text{H}_2)$ information for PGCCs and SDCs, the $A_V(\text{H}_2)$ values of these clouds are directly derived from the $N(\text{H}_2)$ through the transition $A_V(\text{H}_2) = 2N(\text{H}_2) / 1.87 \times 10^{21}$ cm⁻².

OH integrated intensity $W(\text{OH})$ was derived by summing the emission together along a line of sight. For SDCs with OH absorptions, we utilized the absolute intensity value of each component.

In Figure 6, we plot the the relation between OH intensity of 1667 MHz line, $W(\text{OH})$ and $A_V^{\text{H}_2}$ along the

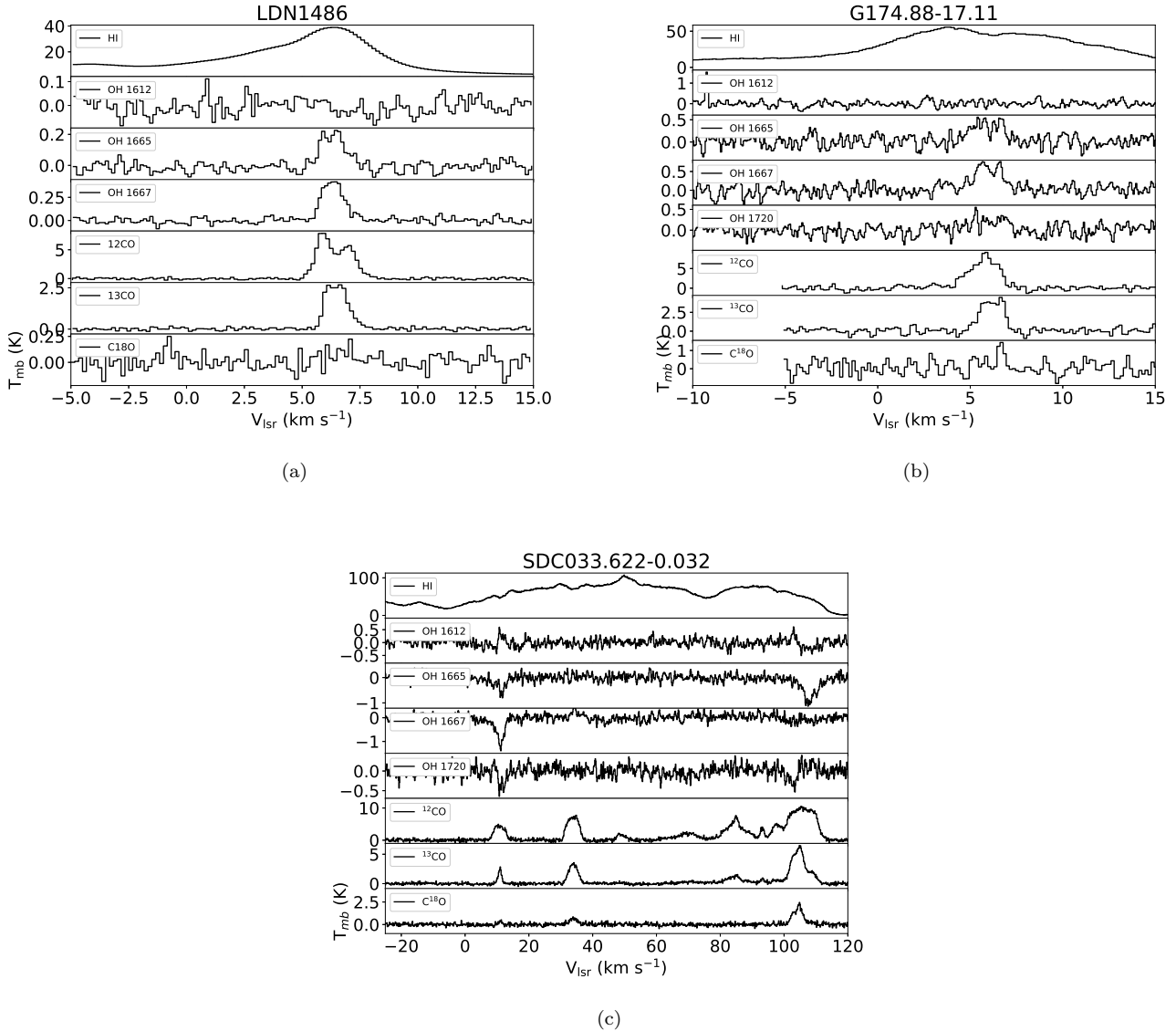


Figure 3. HI, OH and CO spectra toward LDN1486 (ODCs), G174.88-17.11 (PGCCs) and SDC033.622-0.032 (SDCs). The continuum levels of these spectra were fitted and subtracted.

sightline of three categories of clouds. The $W(\text{OH})$ value of all OH diffuse components was summed together for each sightline. OH maser components are excluded since they significantly deviate from collisional excitation.

As shown in Figure 6, $W(\text{OH})$ correlates with $A_V(\text{H}_2)$ linearly following $W(\text{OH}) = (0.46 \pm 0.06) A_V(\text{H}_2) + (0.28 \pm 0.11)$ when $A_V(\text{H}_2) \leq 3$ mag. It stays almost constant at $A_V(\text{H}_2)$ range of 3 to 7 mag and increases linearly when $A_V(\text{H}_2) > 7$ mag. Cotten et al. (2012) found an empirical relationship between $W(\text{OH})$ and $E(B - V)(\text{H}_2)$, $W(\text{OH}) = (0.71 \pm 0.08)E(B - V)(\text{H}_2) - (0.05 \pm 0.01)$ for the high latitude translucent cloud MBM40 with $E(B - V)(\text{H}_2) \leq 0.17$ mag. We plot this relationship in Figure 6 by assuming the conversion

$A_V/E(B - V) = 3.1$ (Bohlin et al. 1978). The linear relationship is consistent with our data only for $A_V(\text{H}_2) > 7$ mag and exists large discrepancy for the data with low $A_V(\text{H}_2)$.

4.2. OH abundance in molecular clouds

The population of energy levels of OH main lines (1665 and 1667 MHz) is affected a little even there is strong satellite-line anomaly. The intensity of 1667 MHz line is generally larger than that of the 1665 MHz line, leading to a higher signal to noise ratio (SNR) for 1667 MHz line. We calculate OH column density through the emission of 1667 MHz under the assumption of optically thin, which is confirmed by absorptions toward quasars (e.g.,

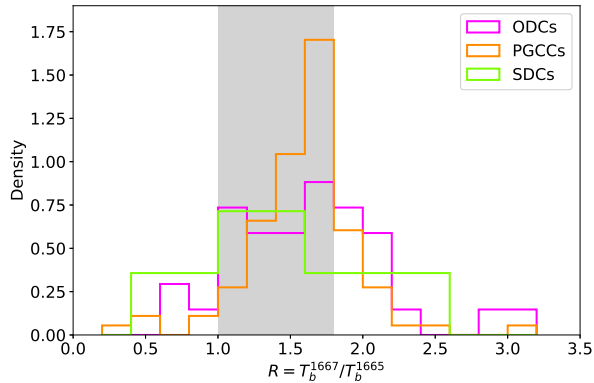


Figure 4. Normalized density distribution of R value for ODCs, PGCCs, and SDCs. The grey shade represents the R range that can be explained by optical depth of OH under LTE.

Li et al. 2018). $N(\text{OH})$ can be derived by use of the formula (e.g., Dickey et al. 1981),

$$N(\text{OH}) = 2.26 \times 10^{14} \frac{1}{f} \frac{T_{\text{ex}}}{T_{\text{ex}} - T_{\text{bg}}} \int T_{\text{mb}} dv \text{ cm}^{-2}, \quad (1)$$

where f is the beam filling factor. It is adopted as 1 since both the major and minor size of the observed sources are larger than the Arecibo beam of $2.7' \times 3.1'$ at 1.6 GHz. The OH absorption region may be smaller than that of emission, indicating a smaller filling factor and underestimation of $N(\text{OH})$ from absorption compared to that of emission (Engelke & Allen 2019). T_{ex} and T_{bg} are excitation temperature and background temperature of OH 1667 MHz transition, respectively; T_{mb} is the main-beam temperature of 1667 MHz line.

The value of T_{ex} is critical for calculating $N(\text{OH})$. Heiles (1968) derived T_{ex} by assuming local thermal equilibrium (LTE) between OH main lines, which implies $T_{1667}^{\text{ex}} = T_{1665}^{\text{ex}}$ and $\tau_{1667} = 1.8\tau_{1665}$. The brightness temperature ratio ($R = T_b^{1667}/T_b^{1665}$) approaches 1 when $\tau_{1667} \gg 1$ and 1.8 when $\tau_{1667} \ll 1$. Absorptions toward continuum sources convinced significant deviation of LTE even R lies in the range of [1.0, 1.8] at small optical depth (Crutcher 1979; Dickey et al. 1981; Li et al. 2018). The adoption of LTE condition by assuming same excitation temperature of two main lines would lead to an overestimation of optical depth and then OH column density by more than one order of magnitude (e.g., Crutcher 1977).

Explicit measurement of T_{ex} were conducted through absorption/emission toward quasars (Dickey et al. 1981; Liszt & Lucas 1996; Li et al. 2018) and grid mapping to-

ward a continuum background, e.g., star-forming region (Engelke & Allen 2018).

Due to lack of independent measurement of T_{ex} for our sources, we estimated the value of $T_{\text{ex}}/(T_{\text{ex}}-T_{\text{bg}})$ through Monte Carlo simulation based on the fitted T_{ex} profile in Li et al. (2018) in the section 6.4. Though there is no physical correlation between T_{ex} and T_{bg} , the average value of $T_{\text{ex}}/(T_{\text{ex}}-T_{\text{bg}})$ is consistent with the result by adopting the value of $|T_{\text{ex}}-T_{\text{bg}}| = 2.03$ K. Since there is no direct measurement of continuum temperature with Arecibo telescope, the value of T_{bg} of each source was calculated through the equation $T_{\text{bg}} = 2.73 + (T_{\text{bg}408} - 2.73)(\nu_{\text{OH}}/408\text{MHz})^{-2.7}$, in which $T_{\text{bg}408}$ is derived from the 408 MHz survey (Haslam et al. 1982). The value of T_{bg} ranges from 3.1 to 13.3 K, resulting in $T_{\text{ex}}/(T_{\text{ex}}-T_{\text{bg}})$ range of [2.6, 7.7]. Uncertainties during the calculations are discussed in the section 6.4.

Both radio and UV observations suggest that OH abundance $X(\text{OH})$ relative to H_2 (e.g., Magnani & Siskind 1990; Liszt & Lucas 1996; Weselak et al. 2010; Xu et al. 2016; Nguyen et al. 2018) ranges from 8×10^{-9} to 4×10^{-6} and approaches 10^{-7} . The $X(\text{OH})$ range in our survey is from 5.7×10^{-8} to 4.8×10^{-6} , which is consistent with previous observations.

Besides, the possible decreasing trend of $X(\text{OH})$ in denser regions is suggested in previous observations. To investigate this in details, we plot $X(\text{OH})$ as a function of visual extinction A_V in Figure 7. $X(\text{OH})$ stays almost constant before decreasing $A_V \sim 1.5$ mag. It saturates again when $A_V > 10$ mag. Xu et al. (2016) found an empirical relationship between $X(\text{OH}) = [\text{OH}]/[\text{H}_2]$ and A_V across the boundary of Taurus molecular cloud, $X(\text{OH}) = 1.5 \times 10^{-7} + 9.0 \times 10^{-7} \times \exp(-A_V/0.81)$, which is valid for A_V range of 0.4 to 2.7 mag. As a comparison, we plot this relationship in Figure 7. It is obvious that the trend of the bin data is consistent with the relationship from Xu et al. (2016), but there exists significant discrepancy in the turn-off points. Inspiring by this fact, we fitted the bin data with same formula in Xu et al. (2016) and found the relationship follows,

$$\frac{X(\text{OH})}{10^{-7}} = 1.3_{-0.4}^{+0.4} + 6.3_{-0.5}^{+0.5} \times \exp\left(-\frac{A_V}{2.9_{-0.6}^{+0.6}}\right). \quad (2)$$

As for chemistry evolution from the model, van Dishoeck & Black (1986) presented OH abundances ranging from 1.1×10^{-9} to 6.7×10^{-8} under 19 models with different density, kinetic temperature and visual extinction in diffuse and translucent clouds. The visual extinction of all models ranges from 0.64 to 1.01 mag expect one with $A_V = 2.12$ mag. There is no obvious decreasing trend of $X(\text{OH})$ along with A_V from

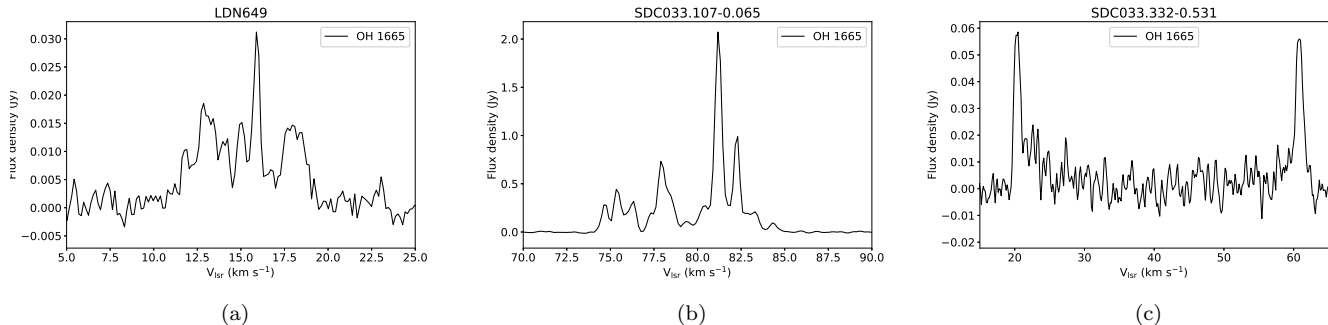


Figure 5. Detected OH masers. The flux density was converted from antenna temperature by dividing the Arecibo gain of 10 K/Jy.

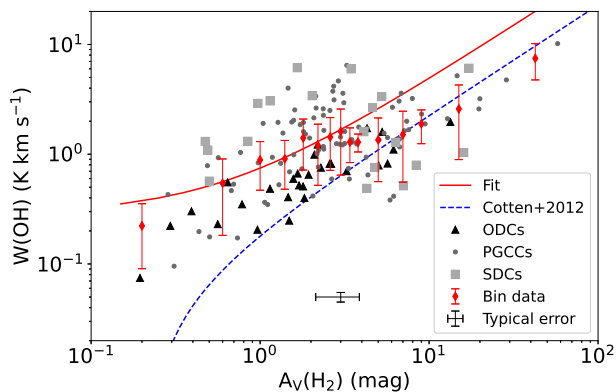


Figure 6. The relationship between $W(\text{OH})$ and A_V . The data were binned with width of 0.4, 2 and 10 mag for $A_V(\text{H}_2)$ range of [0, 4] mag, [4, 10] mag and [10, 20] mag, respectively. The bin data at $A_V(\text{H}_2)=42.5$ mag is derived for the data with $A_V(\text{H}_2)$ range of [20, 65] mag. Red solid line represents linear fit of bin data with $A_V \leq 3$ mag. The correlation derived by Cotten et al. (2012) is shown with blue dashed line. This correlation is valid for $E(B-V)(\text{H}_2)$ range of [0.08, 0.17] mag, which corresponds to $A_V(\text{H}_2)$ range of [0.25, 0.53] mag when $A_V/E(B-V)=3.1$ was adopted.

these modeling results. The reason may due to limited A_V range and varied density and kinetic temperature. Lee et al. (1996) conducted photodissociation region (PDR) simulations of a static, plane-parallel, semi-infinite cloud with constant temperature of 30 K and density profile that represents self gravitating isothermal sphere. In the steady state of the simulations, OH abundance increases with A_V at $A_V < 4$ mag and then decreases when $A_V > 4$ mag. The peak is $\sim 8 \times 10^{-8}$ corresponding to $A_V = 4$ mag.

Bialy & Sternberg (2015) found a maximum OH abundance of $\sim 6 \times 10^{-7}$ near the H-to- H_2 conversion region under low metallicities environment. In the H_2 dominated region, OH abundance decrease linearly as

increasing ζ/n , in which ζ and n are the cosmic ray ionization rate and total hydrogen density, respectively. As pointed out by the authors, this result is limited to the situations of low metallicities since the dust-grain formation of the heavy molecules is neglected. Hollenbach et al. (2012) described the detailed chemistry evolution in molecular clouds when polycyclic aromatic hydrocarbons (PAHs) were included in a steady-state PDR model. The OH abundance shows a peak of $\sim 3 \times 10^{-6}$ at a A_V^{crit} value, which depends on the inputting parameters in the model. $A_V^{\text{crit}} \sim 5$ mag when hydrogen density $n = 10^4 \text{ cm}^{-3}$, UV intensity $\chi = 100$ and cosmic-ray ionization rate $\zeta = 2 \times 10^{-16}$.

In a summary, the decreasing trend and saturation feature when $A_V > 1.5$ mag in our data is consistent with previous model predictions. The increasing trend in predicted models at lower visual extinction (e.g., $A_V < 1.5$ mag) is not clearly seen in this study. One possible explanation is that model always assume ‘fixed’ physical parameters (e.g., temperature, density-extinction relation) which are unreasonable for analyzed clouds with totally different environments. Further quantitative comparison between the results and PDR models are needed.

4.3. OH versus CO

CO is the most common probe for tracing H_2 in molecular regions. CO spectral surveys (e.g., Wu et al. 2012) toward dark clouds and dark clumps provide a direct statistics of star formation process. The J= 1-0 transition line of ^{13}CO emission is optically thin even in cloud with extinction of 10 mag. It was detected toward most of the components with OH detection. We compare the ^{13}CO intensity $W(^{13}\text{CO})$ with the $W(\text{OH})$ in Fig. 8. We can see that $W(^{13}\text{CO})$ correlates linearly with $W(\text{OH})$ following the equation, $W(^{13}\text{CO}) = (2.49 \pm 0.40)W(\text{OH}) + (1.72 \pm 1.26)$.

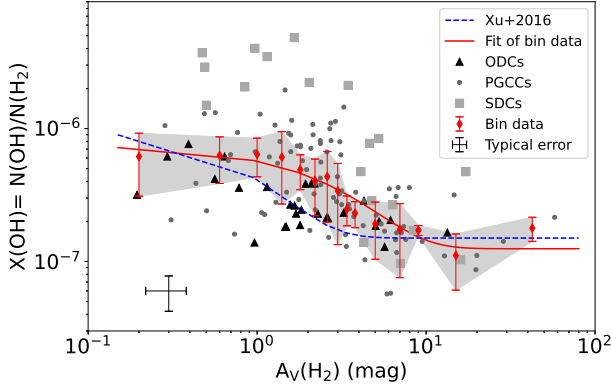


Figure 7. The relationship between OH abundance and A_V . The range of bin data is the same as that in Fig. 6. The relationship found in Xu et al. (2016) is shown with blue dashed line. Fitting result of the bin data is shown with red solid line. As shown in Section 6.4, OH column density was calculated from the intensity of OH 1667 line by adopting excitation temperature derived from Monte Carlo simulations with one sigma uncertainty.

The column density $N(^{13}\text{CO})$ of ^{13}CO is calculated with the following equation,

$$N(^{13}\text{CO}) = 2.42 \times 10^{14} \frac{T_x \tau^{13} \Delta V^{13} / 0.937}{1.0 - e^{-5.29/T_x}} \text{cm}^{-2}, \quad (3)$$

where T_x is excitation temperature of ^{13}CO . It was derived by assuming same excitation temperature of ^{12}CO and ^{13}CO and optically thick of ^{12}CO emission. $T_x = 5.532 / \ln(1 + 5.532 / (T_b^{12} + 0.819))$, in which T_b^{12} is the brightness temperature of ^{12}CO . The ^{13}CO optical depth $\tau^{13} = -\log(1 - T_b^{13} / 5.29 / J(T_x) - 0.164)$, in which T_b^{13} the brightness temperature of ^{13}CO and $J(T_x) = 1 / (\exp(5.29/T_x) - 1)$.

The $N(\text{OH})/N(^{13}\text{CO})$ ratio as a function of $A_V(\text{H}_2)$ is shown in Figure 9. The $N(\text{OH})/N(^{13}\text{CO})$ ratio increases when $A_V(\text{H}_2) < 2$ mag. It decreases until saturation at $A_V(\text{H}_2) = 8$ mag.

5. RELATIONSHIP BETWEEN OH AND HINSA IN TRACING MOLECULAR GAS

HINSA is widely used in tracing the cold HI inside a molecular cloud. It was found to be associated with molecular emissions in dark clouds (Li & Goldsmith 2003; Krčo & Goldsmith 2010). A total of 70 OH components are associated with HINSA feature. An example of HINSA is shown around 5.8 km s^{-1} in Fig. 3(b).

By adopting the radiation geometry in Li & Goldsmith (2003), ‘expected’ HI profile without

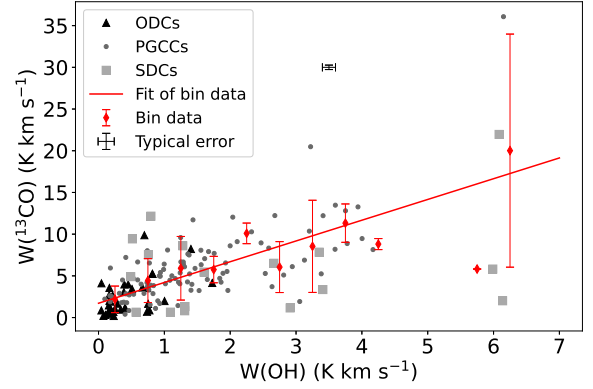


Figure 8. The relationship between intensity of OH and ^{13}CO . The data were divided into bins with width of 0.5 km s^{-1} . The fitting result of bin data is shown with red solid line.

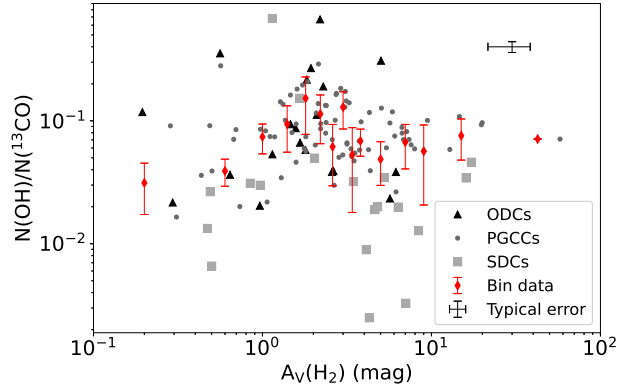


Figure 9. The relationship between $N(\text{OH})/N(^{13}\text{CO})$ ratio and A_V . The range of bin data is the same as that in Fig. 6.

absorption can be expressed with the following equation,

$$T_{\text{HI}} = \frac{T_{\text{R}} + (T_{\text{c}} - T_{\text{k}})(1 - \tau_f)(1 - e^{-\tau})}{1 - p(1 - e^{-\tau})} \quad (4)$$

where T_{c} represents the background continuum temperature contributed by the cosmic background and the Galactic continuum emission, T_{k} is the excitation temperature of the atomic hydrogen in the cold cloud, which is equal to the kinetic temperature, τ is the optical depth of the cold cloud. τ_f and τ_b are the optical depths of warm HI gas in front and behind the HINSA cloud. The total optical depth of warm HI gas along the line of sight is $\tau_h = \tau_f + \tau_b$. p is defined as the fraction of background HI, $p = \tau_b / \tau_h$. The value of p depends on the spatial location of the absorption cloud, which is determined by

galactic longitude l , galactic latitude b and distance d from the observer. Due to the difficulty in measuring cloud distance directly, we introduce kinematic distance d_{kin} which could be calculated through its velocity (V_{cen}) after applying rotational curve. Thus the value of p is a function of l , b , and V_{cen} , with $p = p(l, b, V_{\text{cen}})$.

Once the cloud position is determined, three dimensional distribution of Galactic HI is necessary to calculate p . Kalberla & Dedes (2008) derived midplane HI volume density distribution $n(R, z_0)$ and HI average thickness distribution b_R as a function of Galactocentric radius R based on HI surveys. The descriptions of $n(R, z_0)$ and $b_z(R)$ are shown in the following formula,

$$n(R, z_0) \sim n_0 e^{-(R-R_\odot)/R_n}, \quad 7 \leq R \leq 35 \text{ kpc}, \quad (5)$$

where $n_0 = 0.9 \text{ cm}^{-3}$, $R_n = 3.15 \text{ kpc}$,

$$b_z(R) \sim b_0 e^{-(R-R_\odot)/R_0}, \quad 5 \leq R \leq 35 \text{ kpc}, \quad (6)$$

where $b_0 = 0.15 \text{ kpc}$, $R_0 = 9.8 \text{ kpc}$.

By simply adopting a gaussian distribution along z axis, we constructed a 3-D volume density distribution $n(R, z)$ of HI, which can be described with

$$n(R, z) = n(R, z_0) e^{-z^2/b_z^2(R)}. \quad (7)$$

With this distribution, we calculated the value of p by considering integrated HI content along the line-of-sight (LOS) of molecular cloud.

The value of p is 0.81 for LDN621. As shown in Table 3 and Fig. 10, the HINSA column density ranges from 2×10^{17} to $2 \times 10^{19} \text{ cm}^{-2}$, with a median value of $2.3 \times 10^{18} \text{ cm}^{-2}$.

As for the column density relationship between OH and HINSA, HINSA column density $N(\text{HINSA})$ stays almost constant when $N(\text{OH}) < 2.5 \times 10^{15} \text{ cm}^{-2}$.

6. DISCUSSION

6.1. Non-thermal Velocity Dispersions between OH, CO and HINSA

Non-thermal velocity broadening in molecular cloud is mainly caused by turbulence. Investigating the non-thermal line dispersion (σ_{NT}) is beneficial to reveal kinematical behavior for different tracers. We calculate σ_{NT} with the following equation,

$$\sigma_{\text{NT}} = \sqrt{\sigma_{\text{obs}}^2 - \sigma_{\text{TH}}^2}, \quad (8)$$

in which $\sigma_{\text{obs}} = \Delta V_{\text{FWHM}}/8\ln(2)$ is the observed line dispersion. $\sigma_{\text{TH}} = \sqrt{kT_k/m_H\mu}$ is the thermal velocity dispersion of the tracer. k , T_k , m_H and μ are the Boltzmann constant, kinetic temperature, the mass of proton, and molecular weight of the tracer, respectively.

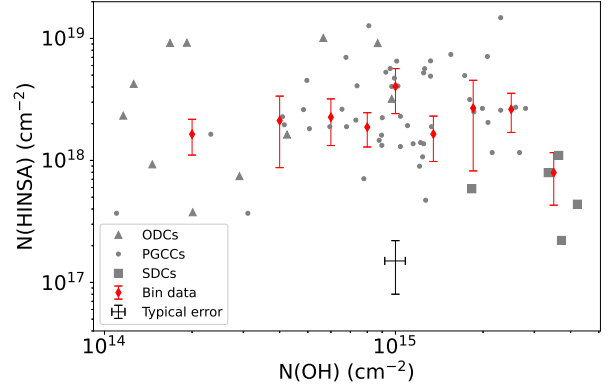


Figure 10. Relation between HINSA and OH column density. The X values of bin data are [2, 4, 6, 8, 10, 13.5, 18.5, 25, 35] $\times 10^{14} \text{ cm}^{-2}$. The limits of X bin data are [1, 3, 5, 7, 9, 11, 16, 21, 30, 40] $\times 10^{14} \text{ cm}^{-2}$.

By adopting isothermal assumption of the ISM, we calculated the nonthermal velocity dispersions for ^{13}CO , OH and HINSA based on estimated value of T_k from CO observations. Nonthermal velocities are generally less than 1.5 km s^{-1} , consistent with previous CO observations (e.g., analysis of PGCCs in Wu et al. (2012)). Their relationships are shown in Fig. 11.

As shown in Fig. 11(a), $\sigma_{\text{NT}}^{\text{OH}}$ is closely correlated with $\sigma_{\text{NT}}^{\text{CO}}$, implying similar volume occupation for OH and ^{13}CO in space. The averaged value of $\sigma_{\text{NT}}^{\text{OH}}$ is $\sim 0.12 \text{ km s}^{-1}$ smaller than that of $\sigma_{\text{NT}}^{\text{CO}}$. Barriault et al. (2010) found broader nonthermal line width of OH compared to ^{12}CO in cirrus clouds with high Galactic latitude. The discrepancy between our result and that in Barriault et al. (2010) may arise from limited sample in Barriault et al. (2010).

No clear correlation is found for the nonthermal velocity dispersion between OH and HINSA. The values of $\sigma_{\text{NT}}^{\text{OH}}$ are larger than that of $\sigma_{\text{NT}}^{\text{HINSA}}$ in most clouds. Combined with the relationship between $N(\text{OH})$ and $N(\text{HINSA})$, OH and HINSA may occupy different volumes of space along sightline.

In short, the averaged nonthermal dispersions follow $\sigma_{\text{NT}}^{\text{CO}} > \sigma_{\text{NT}}^{\text{OH}} > \sigma_{\text{NT}}^{\text{HINSA}}$. The result of $\sigma_{\text{NT}}^{\text{CO}} > \sigma_{\text{NT}}^{\text{HINSA}}$ is consistent with that found in Tang et al. (2020).

6.2. Cloud Age and Time dependent OH Abundance

HI Narrow Self-Absorption (HINSA) appears if there exists a warmer HI background against the cold HI gas along sightline. With an abundance of $\sim 10^{-2.8}$ (e.g., Krčo & Goldsmith 2010) observed in HINSA survey of dark clouds, HINSA is another effective tracer of cold molecular gas in diffuse and dense molecular cloud.

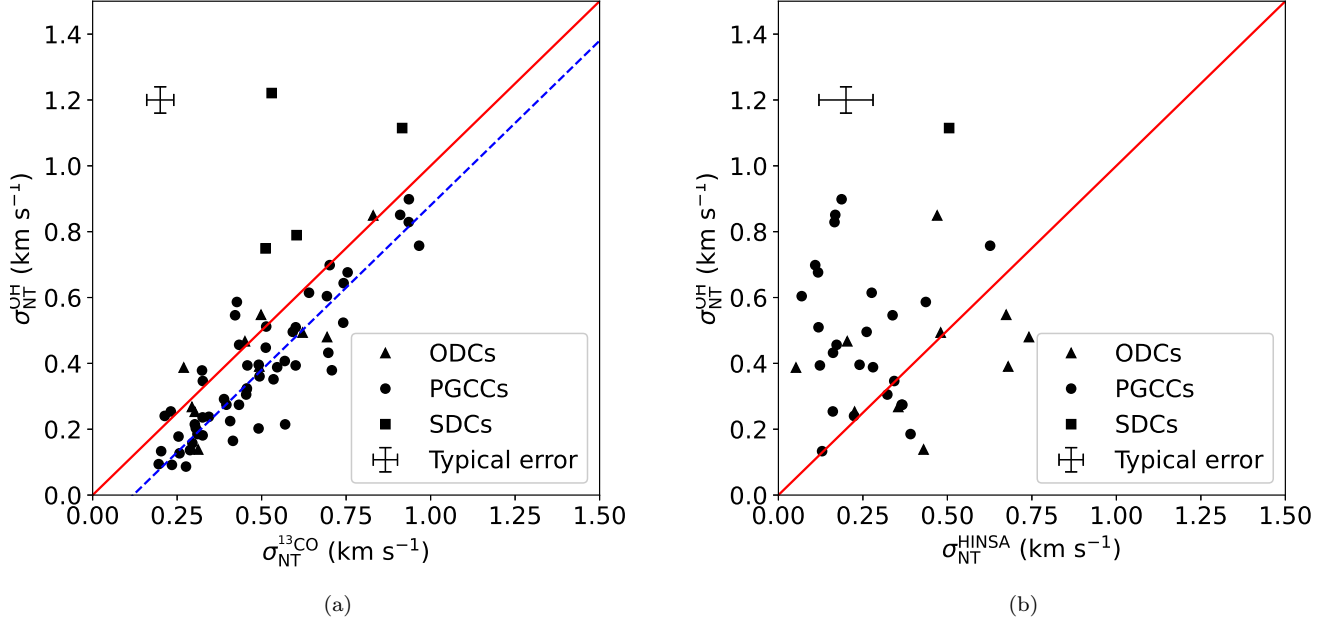


Figure 11. Comparison of nonthermal velocity dispersions of different molecular tracers. (a): OH versus ^{13}CO . The red solid and blue dashed lines represent $\sigma_{\text{NT}}^{\text{OH}} = \sigma_{\text{NT}}^{^{13}\text{CO}}$ and $\sigma_{\text{NT}}^{\text{OH}} = \sigma_{\text{NT}}^{^{13}\text{CO}} - 0.12 \text{ km s}^{-1}$, respectively. (b): OH versus HINSAs. The red solid represents $\sigma_{\text{NT}}^{\text{OH}} = \sigma_{\text{NT}}^{\text{HINSAs}}$.

HINSAs located in the central core of molecular clouds is balanced by formation through H_2 dissociation from cosmic ray and depletion of HI-H_2 transition. Thus it is a perfect tracer of the cloud ‘age’, which indicates transition process between atomic and molecular gas.

We adopted the same analysis method of cloud age in Goldsmith & Li (2005). Time dependent HI fraction is given by

$$x_1(t) = 1 - \frac{2k'n_0}{2k'n_0 + \zeta_{\text{H}_2}} \left[1 - \exp\left(\frac{-t}{\tau_{\text{HI} \rightarrow \text{H}_2}}\right) \right] \quad (9)$$

in which k' and n_0 are the formation rate coefficient of H_2 and total proton density respectively. Grain size distribution would increase the formation rate coefficient by a factor of 3.4, thus we adopt the nominal value $k' = 1.2 \times 10^{-17} \text{ s}^{-1}$ (Goldsmith & Li 2005). ζ_{H_2} is the ionization rate of H_2 by cosmic-ray, whose value ranges from 10^{-17} to 10^{-15} s^{-1} in dense and diffuse Galactic clouds (e.g., Federman et al. 1996; van der Tak & van Dishoeck 2000; Bialy et al. 2019), and even reaches 10^{-14} s^{-1} in the Galactic center (Le Petit et al. 2016). The time scale for atomic-molecular hydrogen conversion $\tau_{\text{HI} \rightarrow \text{H}_2}$ is described by

$$\tau_{\text{HI} \rightarrow \text{H}_2} = \frac{1}{2k'n_0 + \zeta_{\text{H}_2}}. \quad (10)$$

The uncertainty of ζ_{H_2} has less effect for the analysis since the densities of clouds are larger than that of 500 cm^{-3} and thus the term $2k'n_0 \gg \zeta_{\text{H}_2}$ in Equation 9 and 10. We adopted the value $\zeta_{\text{H}_2} = 5.2 \times 10^{-17} \text{ s}^{-1}$ from van der Tak & van Dishoeck (2000) during calculation.

Total proton volume density $n_0 = n_{\text{HI}} + 2n_{\text{H}_2}$ is necessary to solve Equation 9. Thirty one PGCCs with both HINSAs detection and measured n_{H_2} values from Planck survey (Planck Collaboration et al. 2016) exist. Since the size of HI emission is not available for each cloud, we adopt the reasonable assumption $n_{\text{HI}} \ll n_{\text{H}_2}$ due to the fact that $N(\text{HINSAs}) \ll N(\text{H}_2)$ (e.g., Goldsmith & Li 2005). Solutions of Equation 9 are available for 27 of 31 sources. As shown in Figure 12, the cloud ages of these sources range from $10^{5.5}$ to $10^{6.7}$ Myr. Most clouds are still undergoing HI-H_2 transition and do not reach the steady state.

With the information of cloud age, it is available to derive the OH abundance as a function of time. This is important for comparison with time-dependent chemical model. The time-dependent OH abundance is presented in Fig. 13. An obvious increasing trend was found for OH abundance during the time range of [0.29, 5.0] Myr.

We fit the results with a linear function. Best fitting parameters are described with

$$\frac{X(\text{OH})}{10^{-8}} = (7.0 \pm 1.8) \times \frac{\tau_{\text{cloud}}}{\text{Myr}} + (6.7 \pm 3.7). \quad (11)$$

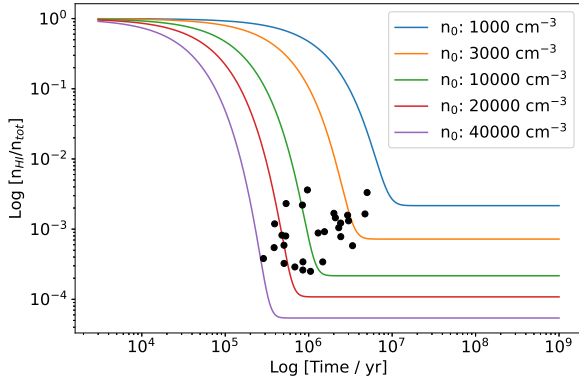


Figure 12. Cloud age for PGCCs. Solid lines represent HI abundance as a function of cloud time in different proton densities, 1×10^3 , 3×10^3 , 1×10^4 , 2×10^4 , and $4 \times 10^4 \text{ cm}^{-3}$.

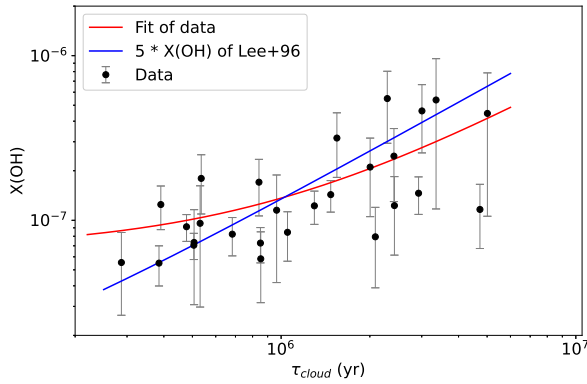


Figure 13. Relationship between OH abundance $X(\text{OH})$ and cloud age τ_{cloud} . The red line represents the fitting with linear function $X(\text{OH}) = a * \tau_{\text{cloud}} + b$, in which $a = (7.0 \pm 1.8) \times 10^{-14}$ and $b = (6.7 \pm 3.7) \times 10^{-8}$. The blue solid line represents the simulation results from Lee et al. (1996). A factor of 5 was multiplied to compare with our data.

Based on PDR simulations of a static, plane-parallel, semi-infinite cloud, Lee et al. (1996) calculated time-dependent OH abundance and found a linear correlation between OH abundance and evolution time. This is valid for A_V range from 1.5 to 10 mag (maximum value of simulation, see Fig. 6a for details). In order to compare our data with this simulation, we fit a linear function of the OH abundances at age of $10^{4.5}$, 10^5 , $10^{5.5}$ and 10^6 yr under the Model 1 (data are derived from Table 3 of Lee et al. 1996). As shown in Fig. 13, our fitting is consistent with time-dependent simulation results except a factor of 5 in amplitude.

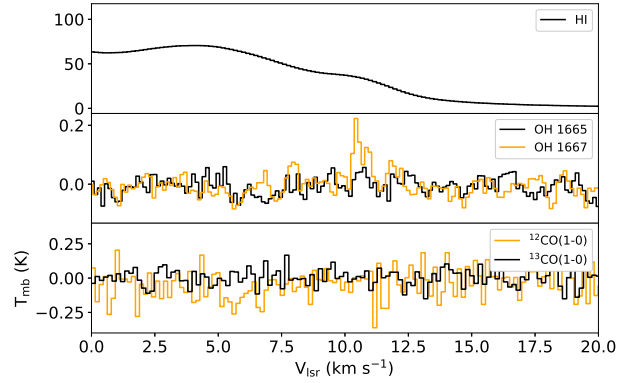


Figure 14. Example of DMG detection toward LDN1525. The signal/noise ratio of OH 1667 emission at 10.2 km s^{-1} is ~ 5 .

6.3. OH as Tracer of Dark Molecular Gas

As a progenitor of CO formation, OH is considered as an effective tracer of ‘CO-dark’ molecular gas (DMG). This has been convinced by amount of Galactic OH surveys (e.g., Allen et al. 2012, 2015; Tang et al. 2017; Busch et al. 2019), Galactic OH absorptions toward Quasars (Li et al. 2018) or continuum sources (Rugel et al. 2018), and envelope of molecular clouds (e.g., Cotten et al. 2012; Xu et al. 2016).

In this survey, we also detected 14 DMG components, which show OH emission but lack corresponding CO emission. As shown in Fig. 14, an example of DMG happens for the OH 1667 emission with peak of 0.2 K at $\sim 10.2 \text{ km s}^{-1}$ toward LDN1425. These detections convince the validity of OH in tracing DMG.

More cases were found toward CO emission without corresponding OH emission. This fact does not challenge the above conclusion and is understandable since OH excitation temperature is tightly close to the background temperature. High sensitivity (e.g, rms of $\sim 3 \text{ mK}$; Allen et al. 2015) leads to a large possibility in detecting OH emission toward DMG. In this work, OH sensitivity is only $\sim 42 \text{ mK}$ for ODC and $\sim 88 \text{ mK}$ for PGCCs and SDCs and gives a detection fraction of 7.3%.

6.4. Uncertainties

During the above analysis, measurement uncertainties from the data are transferred into each variable by error propagation. Besides, a series of uncertainties concerning about the calculation of $N(\text{OH})$ and $N(\text{H}_2)$ exist. They are described as follows.

1. The uncertainty during estimating continuum temperature T_C . The continuum value we estimated in this paper is derived from the 408 MHz

- survey by adopting an power law index of -2.7. This would certainly affect our calculation of continuum temperature at 1.6 GHz for two reasons: (a) The spatial resolution of 51' of 408 MHz survey is much larger than that of Arecibo beam of 3.1' during observations; (b) The continuum contribution of H II region may dominate around the Galactic plane, especially for sources at the first quarter. As a rough check of the uncertainty, the continuum level of spectral bandpass ($T_{\text{cont}}^{\text{bp}}$) of SDC033.382+0.204 (gl, gb = 33.382,0.204) is 36 K while it is 28 K for OFF plane source G049.76-07.25. It is difficult for us to tell the absolute continuum level toward the source due to lack of observation of a 'clean' OFF position. The value of $T_{\text{cont}}^{\text{bp}}$ includes three main parts, $T_{\text{cont}}^{\text{bp}} = T_{\text{sys}} + T_{\text{sky}}$, in which T_{sys} and T_{sky} represents system temperature of the telescope and sky temperature. The value of T_{sys} depends on azimuth and zenith angle of the telescope. The minimum and maximum of T_{sys} values are ~ 22 K and ~ 27 K when a upper limit of 5 K is adopted. Thus the continuum temperature ranges of SDC033.382+0.204 and G049.76-07.25 are [9, 14] K and [1, 6] K. Our adopted T_{C} value of SDC033.382+0.204 ($T_{\text{C}}=13.0$ K) and G049.76-07.25 ($T_{\text{C}}=4.7$ K) locate in the value range from bandpass estimations.
- The uncertainty of $R = T_{\text{ex}}/(T_{\text{ex}} - T_{\text{bg}})$. As described in section 4.2, the R value ranges from 2.6 to 7.7 under the adoption of $|T_{\text{ex}} - T_{\text{bg}}| = 2.03$ K for all sources. To check the validity and uncertainty of this adoption, we took Monte Carlo simulation and generated a sample of T_{ex}^{1667} that ranges from 3.0 to 25 K and satisfies the density probability formula, $\frac{1}{\sqrt{2\pi}\sigma} \exp\left[-\frac{[\ln(T_{\text{ex}}) - \ln(3.4 \text{ K})]^2}{2\sigma^2}\right]$, in Li et al. (2018). The detection of OH emission implies the equation $T_{\text{ex}} > T_{\text{bg}}$. We assumed a lower limit of difference of 0.1 K, $T_{\text{ex}} - T_{\text{bg}} > 0.1$ K, which is reasonable and may be underestimated for rms of 0.044 K in obtained spectrum. As shown in Fig. 15, our adopted values are consistent the averaged value from Monte Carlo simulation when $T_{\text{bg}} < 13$ K. The uncertainty of this adoption is large and may affect the calculation of N(OH).
 - The uncertainty of conversion factor between proton column density and A_{V} . Nguyen et al. (2018) derived $N_{\text{H}}/E(\text{B-V}) = (9.4 \pm 1.6) \times 10^{21} \text{ cm}^{-2} \text{ mag}^{-1}$ for pure HI sightlines at high latitude ($|b| > 5$ deg). This value is 60% higher than the canonical value $N_{\text{H}}/E(\text{B-V}) = 5.8 \times 10^{21} \text{ cm}^{-2} \text{ mag}^{-1}$ (Bohlin et al. 1978), which includes the contribu-

tion of both atomic and molecular gas. For this consideration, we adopted the canonical value to derive N(HI) and N(H₂) for SDC clouds without direct N(H₂) measurements in the Galactic plane. But we note that the derived X(OH) would be 38% lower when the conversion factor in Nguyen et al. (2018) was adopted.

7. SUMMARY

An OH 18 cm survey toward 33 ODCs, 98 PGCCs and 10 SDCs were made with Arecibo telescope. With visual extinction ranging from 0.3 to 60 mag, these sources have different stages of cloud evolution. The survey toward these source reveals a comprehensive OH excitation and chemical evolution of molecular tracers for star formation. Our results are summarized as follows.

- A large fraction of OH components have 1667/1665 ratio range deviating from the thermal ratio range of [1.0, 1.8], implying common non-thermal excitation in ODCs, PGCCs and SDCs.
- The infrared radiation from nearby YSOs, IR or FIR targets is not necessary to generate OH satellite anomaly except for the satellite anomaly with 'conjugate' feature, which is always caused by infrared pumping.
- OH intensity shows a linear correlation with visual extinction (Figure 6), $W(\text{OH}) = (0.46 \pm 0.06)A_{\text{V}} + (0.28 \pm 0.11)$ when $A_{\text{V}} < 3$ mag. When $A_{\text{V}} > 7$ mag, $W(\text{OH})-A_{\text{V}}$ correlation follows the linear relationship of Cotten et al. (2012).
- OH column density was calculated from the intensity of OH 1667 line by adopting excitation temperature derived from Monte Carlo simulations with one sigma uncertainty. The adoption of $|T_{\text{ex}} - T_{\text{bg}}| = 2.03$ K is consistent with the average results of Monte Carlo simulations.
- The OH abundance was found to decrease with increasing visual extinction A_{V} (Figure 7),

$$\frac{X(\text{OH})}{10^{-7}} = 1.3_{-0.4}^{+0.4} + 6.3_{-0.5}^{+0.5} \times \exp\left(-\frac{A_{\text{V}}}{2.9_{-0.6}^{+0.6}}\right),$$

consistent with PDR models.

- ¹³CO intensity increases linearly with OH intensity following $W(^{13}\text{CO}) = (2.49 \pm 0.40)W(\text{OH}) + (1.72 \pm 1.26)$ (Figure 8).

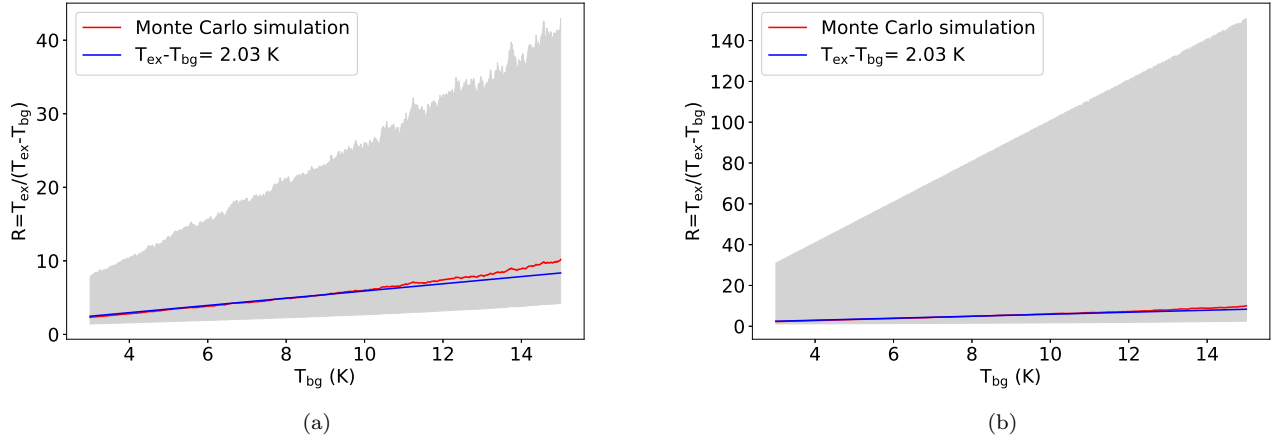


Figure 15. The relationship between R and T_{bg} . The results from Monte Carlo simulation and adoption of $|T_{\text{ex}} - T_{\text{bg}}| = 2.03$ K are shown with red and blue solid lines, respectively. The uncertainties with 66.7% probability and 100% probability from Monte Carlo simulation are shown in (a) and (b) with grey shade, respectively.

7. HINSA was detected toward 70 OH components. The column density of HINSA locates in the $[2 \times 10^{17}, 2 \times 10^{19}] \text{ cm}^{-2}$ and has a median value of $2.3 \times 10^{18} \text{ cm}^{-2}$. HINSA column density stays almost constant when $N(\text{OH}) < 2.5 \times 10^{15} \text{ cm}^{-2}$ (Figure 10).
8. Nonthermal velocity dispersion of OH is found to closely correlated with that of ^{13}CO (Figure 11a), indicating their being occupying similar spatial volumes. No obvious correlation is found between nonthermal velocity dispersion of OH and HINSA (Figure 11b).
9. Based on HINSA analysis of cloud age of 27 PGCCs with explicit density measurements, the relationship between OH abundance $X(\text{OH})$ and cloud age τ_{cloud} follows a linear function (Figure 13),

$$\frac{X(\text{OH})}{10^{-8}} = (7.0 \pm 1.8) \times \frac{\tau_{\text{cloud}}}{\text{Myr}} + (6.7 \pm 3.7), \quad (12)$$

which is consistent with time-dependent PDR simulations.

ACKNOWLEDGMENTS

We are grateful to the anonymous referee for his/her constructive suggestions, which have greatly improved this paper. This work is supported by the the National Natural Science Foundation of China (Grant No. 11988101, 11803051, and 11725313), National Key R&D Program of China (2017YFA0402600), CAS International Partnership Program (114A11KYSB20160008), CAS “Light of West China” Program. S.-L.Q. is supported by the Joint Research Fund in Astronomy (U1631237) under cooperative agreement between the National Natural Science Foundation of China (NSFC) and Chinese Academy of Sciences (CAS).

CO data were observed with the Delingha 13.7 m telescope of the Qinghai Station of Purple Mountain Observatory. We appreciate all the staff members of the Delingha observatory for their help during the observations.

REFERENCES

- Allen, R. J., Ivette Rodríguez, M., Black, J. H., et al. 2012, *AJ*, 143, 97
- Allen, R. J., Hogg, D. E., & Engelke, P. D. 2015, *AJ*, 149, 123
- Barriault, L., Joncas, G., Lockman, F. J., et al. 2010, *MNRAS*, 407, 2645
- Bialy, S., Neufeld, D., Wolfire, M., et al. 2019, *ApJ*, 885, 109
- Bialy, S. & Sternberg, A. 2015, *MNRAS*, 450, 4424
- Bohlin, R. C., Savage, B. D., & Drake, J. F. 1978, *ApJ*, 224, 132
- Busch, M. P., Allen, R. J., Engelke, P. D., et al. 2019, *ApJ*, 883, 158
- Cotten, D. L., Magnani, L., Wennerstrom, E. A., et al. 2012, *AJ*, 144, 163
- Crutcher, R. M. 1977, *ApJ*, 216, 308
- Crutcher, R. M. 1979, *ApJ*, 234, 881

- Crutcher, R. M. & Watson, W. D. 1976, *ApJ*, 209, 778
Crutcher, R. M. 1973, *ApJ*, 185, 857
Dawson, J. R., Walsh, A. J., Jones, P. A., et al. 2014, *MNRAS*, 439, 1596
Dickey, J. M., Crovisier, J., & Kazes, I. 1981, *A&A*, 98, 271
Dickey, J. M. & Benson, J. M. 1982, *AJ*, 87, 278
Dutra, C. M. & Bica, E. 2002, *A&A*, 383, 631
Ebisawa, Y., Inokuma, H., Sakai, N., et al. 2015, *ApJ*, 815, 13
Engelke, P. D. & Allen, R. J. 2018, *ApJ*, 858, 57
Engelke, P. D. & Allen, R. J. 2019, *ApJ*, 874, 49
Federman, S. R., Weber, J., & Lambert, D. L. 1996, *ApJ*, 463, 181
Goldsmith, P. F. & Li, D. 2005, *ApJ*, 622, 938
Grossmann, V., Heithausen, A., Meyerdierks, H., et al. 1990, *A&A*, 240, 400
Harju, J., Winnberg, A., & Wouterloot, J. G. A. 2000, *A&A*, 353, 1065
Haslam, C. G. T., Salter, C. J., Stoffel, H., et al. 1982, *A&AS*, 47, 1
Heiles, C. 1969, *ApJ*, 157, 123
Heiles, C., Perillat, P., Nolan, M., et al. 2001, *PASP*, 113, 1247
Heiles, C. E. 1968, *ApJ*, 151, 919
Hollenbach, D., Kaufman, M. J., Neufeld, D., et al. 2012, *ApJ*, 754, 105
Kalberla, P. M. W. & Dedes, L. 2008, *A&A*, 487, 951
Krčo, M. & Goldsmith, P. F. 2010, *ApJ*, 724, 1402
Le Petit, F., Ruaud, M., Bron, E., et al. 2016, *A&A*, 585, A105
Lee, H.-H., Herbst, E., Pineau des Forets, G., et al. 1996, *A&A*, 311, 690
Li, D. & Goldsmith, P. F. 2003, *ApJ*, 585, 823
Li, D., Tang, N., Nguyen, H., et al. 2018, *ApJS*, 235, 1
Liszt, H. & Lucas, R. 1996, *A&A*, 314, 917
Litvak, M. M. 1969, *ApJ*, 156, 471
Magnani, L. & Siskind, L. 1990, *ApJ*, 359, 355
Meng, F., Wu, Y., & Liu, T. 2013, *ApJS*, 209, 37
Myers, P. C., Ho, P. T. P., Schneps, M. H., et al. 1978, *ApJ*, 220, 864
Negrello, M., Gonzalez-Nuevo, J., De Zotti, G., et al. 2017, *MNRAS*, 470, 2253
Nguyen, H., Dawson, J. R., Miville-Deschênes, M.-A., et al. 2018, *ApJ*, 862, 49
Peek, J. E. G., Babler, B. L., Zheng, Y., et al. 2018, *ApJS*, 234, 2
Peretto, N., Lenfestey, C., Fuller, G. A., et al. 2016, *A&A*, 590, A72
Peretto, N. & Fuller, G. A. 2009, *A&A*, 505, 405
Planck Collaboration, Ade, P. A. R., Aghanim, N., et al. 2011, *A&A*, 536, A23
Planck Collaboration, Ade, P. A. R., Aghanim, N., et al. 2016, *A&A*, 594, A28
Rugel, M. R., Beuther, H., Bühr, S., et al. 2018, *A&A*, 618, A159
Sancisi, R., Goss, W. M., Anderson, C., et al. 1974, *A&A*, 35, 445
Schultz, G. V. & Wiemer, W. 1975, *A&A*, 43, 133
Schlegel, D. J., Finkbeiner, D. P., & Davis, M. 1998, *ApJ*, 500, 525
Szymczak, M. & Gérard, E. 2004, *A&A*, 414, 235
Tang, N.-Y., Zuo, P., Li, D., et al. 2020, *Research in Astronomy and Astrophysics*, 20, 077
Tang, N., Li, D., Heiles, C., et al. 2017, *ApJ*, 839, 8
Turner, B. E. 1973, *ApJ*, 186, 357
Turner, B. E. & Heiles, C. E. 1974, *ApJ*, 194, 525
van der Tak, F. F. S. & van Dishoeck, E. F. 2000, *A&A*, 358, L79
van Dishoeck, E. F. & Black, J. H. 1986, *ApJS*, 62, 109
Weinreb, S., Barrett, A. H., Meeks, M. L., et al. 1963, *Nature*, 200, 829
Weselak, T., Galazutdinov, G. A., Beletsky, Y., et al. 2010, *MNRAS*, 402, 1991
Wu, Y., Liu, T., Meng, F., et al. 2012, *ApJ*, 756, 76
Xu, D., Li, D., Yue, N., et al. 2016, *ApJ*, 819, 22
Zhang, T., Wu, Y., Liu, T., et al. 2016, *ApJS*, 224, 43

Table 2. Gaussian fitting parameters of OH data.

Srcid	Comp	Name	gl/gb	OH 1665 MHz			OH 1667 MHz				T_{K}	$N(^{13}\text{CO})$	$N(\text{H}_2)$
				T_{peak}	V_{cen}	ΔV	T_{peak}	V_{cen}	ΔV	$N(\text{OH})$			
				K	km s^{-1}	km s^{-1}	K	km s^{-1}	km s^{-1}	10^{14} cm^{-2}			
1	0	CB124	35.12/11.37	0.08 (0.01)	19.30 (0.11)	1.16 (0.26)	0.06 (0.01)	19.50 (0.39)	2.59 (0.71)	1.35 (0.44)	6.96(0.14)	1.67(0.16)	0.28(0.03)
1	1	CB124	35.12/11.37	0.06 (0.03)	20.78 (0.13)	0.76 (0.43)	0.34 (0.25)	8.56(0.10)	6.16(0.24)	0.28(0.03)
2	0	LDN621	35.35/2.34	0.16 (0.01)	12.30 (0.11)	2.19 (0.29)	0.12 (0.01)	12.30 (0.15)	2.18 (0.39)	3.18 (0.69)	3.75(0.31)	2.41(0.25)	4.70(0.47)
2	1	LDN621	35.35/2.34	0.13 (0.02)	14.76 (0.11)	1.37 (0.35)	0.28 (0.02)	14.75 (0.05)	1.30 (0.12)	4.24 (0.49)	4.55(0.29)	0.00(0.00)	4.70(0.47)
2	2	LDN621	35.35/2.34	0.09 (0.02)	16.32 (0.13)	0.92 (0.30)	4.70(0.47)
2	3	LDN621	35.35/2.34	0.07 (0.02)	27.16 (0.18)	1.50 (0.42)	1.27 (0.47)	4.70(0.47)
4	0	CB191	37.56/-6.15	0.09 (0.02)	7.24 (0.12)	0.91 (0.29)	0.80 (0.32)	0.37(0.04)
4	1	CB191	37.56/-6.15	0.07 (0.02)	8.81 (0.15)	1.32 (0.37)	0.21 (0.02)	8.68 (0.05)	0.94 (0.12)	2.01 (0.33)	7.31(0.10)	5.74(0.40)	0.37(0.04)
6	0	LDN638	39.33/3.55	0.07 (0.01)	22.99 (0.20)	2.54 (0.47)	0.05 (0.01)	22.42 (0.32)	3.53 (0.79)	2.03 (0.58)	3.04(0.30)
6	1	LDN638	39.33/3.55	0.07 (0.01)	31.07 (0.18)	2.01 (0.43)	0.09 (0.01)	29.85 (0.23)	5.15 (0.58)	5.04 (0.73)	3.04(0.30)
7	0	LDN640	40.14/-5.01	0.13 (0.01)	8.82 (0.08)	1.67 (0.20)	2.19 (0.35)	6.19(0.07)	0.62(0.16)	0.53(0.05)
9	0	B140	40.68/-3.88	0.12 (0.02)	6.08 (0.10)	1.49 (0.25)	0.13 (0.01)	6.56 (0.16)	2.40 (0.40)	3.60 (0.69)	5.55(0.07)	1.34(0.10)	1.81(0.18)
9	1	B140	40.68/-3.88	0.11 (0.03)	7.48 (0.05)	0.38 (0.13)	0.11 (0.03)	8.26 (0.07)	0.69 (0.21)	0.88 (0.34)	1.81(0.18)
9	2	B140	40.68/-3.88	0.07 (0.02)	26.64 (0.13)	0.87 (0.31)	0.65 (0.30)	1.81(0.18)
9	3	B140	40.68/-3.88	0.06 (0.02)	38.07 (0.15)	0.89 (0.36)	0.58 (0.31)	1.81(0.18)
9	4	B140	40.68/-3.88	0.10 (0.02)	44.39 (0.10)	1.12 (0.24)	1.24 (0.35)	1.81(0.18)
10	0	LDN645	42.66/-2.82	0.22 (0.01)	7.53 (0.06)	1.70 (0.13)	4.19 (0.44)	7.87(0.10)	1.94(0.15)	1.71(0.17)
11	0	LDN649	43.03/-0.67	0.11 (0.01)	19.35 (0.12)	1.87 (0.28)	2.39 (0.47)	12.50(1.25)
11	1	LDN649	43.03/-0.67	0.09 (0.02)	58.39 (0.57)	5.70 (1.41)	0.16 (0.01)	57.38 (0.28)	5.80 (0.57)	10.51 (1.19)	6.71(0.06)	4.29(0.34)	12.50(1.25)
11	2	LDN649	43.03/-0.67	0.06 (0.04)	65.21 (0.42)	1.46 (1.00)	0.11 (0.01)	64.77 (0.45)	6.48 (0.98)	7.72 (1.31)	5.69(0.09)	1.32(0.16)	12.50(1.25)
12	0	IREC58	43.22/8.33	0.11 (0.02)	3.66 (0.09)	0.93 (0.24)	0.15 (0.02)	3.69 (0.10)	0.96 (0.24)	1.26 (0.35)	10.50(0.45)	2.96(0.36)	1.07(0.11)
12	1	IREC58	43.22/8.33	0.15 (0.02)	4.73 (0.06)	0.61 (0.13)	0.26 (0.03)	4.63 (0.05)	0.65 (0.09)	1.46 (0.26)	9.03(0.27)	2.92(0.21)	1.07(0.11)
12	2	IREC58	43.22/8.33	0.09 (0.01)	10.58 (0.11)	1.47 (0.27)	1.16 (0.28)	5.85(0.14)	1.40(0.44)	1.07(0.11)
14	0	LDN658	44.38/-2.33	0.06 (0.02)	7.55 (0.17)	1.27 (0.40)	0.85 (0.35)	1.39(0.14)
14	1	LDN658	44.38/-2.33	0.07 (0.02)	28.73 (0.13)	1.02 (0.31)	0.13 (0.02)	28.27 (0.07)	1.15 (0.17)	1.68 (0.33)	6.71(0.06)	5.09(0.15)	1.39(0.14)
16	0	B335	44.93/-6.55	0.58 (0.03)	8.03 (0.01)	0.34 (0.02)	1.08 (0.03)	8.05 (0.00)	0.34 (0.01)	3.26 (0.14)	9.18(0.24)	13.98(4.44)	5.31(1.69)
16	1	B335	44.93/-6.55	0.51 (0.03)	11.29 (0.01)	0.46 (0.03)	2.08 (0.16)	5.31(1.69)
16	2	B335	44.93/-6.55	0.16 (0.02)	24.73 (0.04)	0.57 (0.10)	0.80 (0.18)	5.31(1.69)
16	3	B335	44.93/-6.55	0.09 (0.02)	38.40 (0.09)	0.90 (0.22)	0.70 (0.23)	5.31(1.69)
18	0	B338	45.53/-8.05	0.07 (0.02)	7.94 (0.12)	0.78 (0.27)	0.08 (0.02)	7.88 (0.10)	0.86 (0.24)	0.58 (0.21)	6.10(0.10)	0.49(0.10)	0.18(0.02)
19	0	LDN672	45.79/-9.04	0.06 (0.02)	20.38 (0.22)	1.89 (0.52)	0.12 (0.02)	20.65 (0.20)	2.64 (0.47)	2.62 (0.62)	0.73(0.07)
20	0	LDN666	45.25/9.11	0.16 (0.06)	5.27 (0.66)	1.80 (0.82)	0.34 (0.02)	5.65 (0.08)	2.01 (0.11)	5.65 (0.47)	7.60(0.07)	5.08(0.21)	1.96(0.20)
20	1	LDN666	45.25/9.11	0.31 (0.15)	6.32 (0.10)	1.12 (0.21)	0.34 (0.04)	6.40 (0.02)	0.68 (0.08)	1.92 (0.30)	8.78(0.08)	1.68(0.15)	1.96(0.20)
21	0	LDN673	46.25/-1.30	0.34 (0.02)	6.88 (0.02)	0.74 (0.05)	0.57 (0.02)	6.94 (0.02)	1.15 (0.04)	7.46 (0.34)	12.56(0.11)	19.46(0.45)	5.76(0.58)
21	1	LDN673	46.25/-1.30	0.07 (0.01)	24.43 (0.20)	2.72 (0.47)	0.11 (0.01)	24.80 (0.15)	3.47 (0.37)	4.35 (0.60)	5.76(0.58)
22	0	LDN1484	165.72/-17.40	0.10 (0.01)	7.10 (0.11)	1.74 (0.28)	0.27 (0.02)	6.88 (0.06)	1.39 (0.13)	2.49 (0.32)	12.22(0.13)	2.66(0.15)	1.37(0.14)
23	0	LDN1485	166.02/-7.66	0.14 (0.02)	-1.69 (0.09)	1.16 (0.23)	1.15 (0.28)	9.28(0.20)	1.50(0.25)	1.47(0.15)
23	1	LDN1485	166.02/-7.66	0.15 (0.02)	-0.49 (0.06)	1.14 (0.15)	0.23 (0.02)	-0.24 (0.05)	0.90 (0.12)	1.49 (0.24)	10.52(0.12)	1.73(0.21)	1.47(0.15)
23	2	LDN1485	166.02/-7.66	0.11 (0.02)	2.00 (0.12)	1.70 (0.30)	1.29 (0.29)	6.30(0.10)	1.29(0.26)	1.47(0.15)
24	0	LDN1486	166.55/-16.64	0.22 (0.02)	6.25 (0.04)	1.15 (0.10)	0.44 (0.02)	6.24 (0.02)	1.08 (0.04)	3.16 (0.17)	9.86(0.20)	5.45(0.18)	1.68(0.17)
25	0	LDN1489	167.96/-19.05	0.06 (0.02)	5.81 (0.06)	0.39 (0.14)	0.06 (0.01)	5.72 (0.11)	0.66 (0.26)	0.26 (0.12)	10.03(0.30)	1.61(0.13)	0.90(0.09)
25	1	LDN1489	167.96/-19.05	0.17 (0.01)	6.65 (0.02)	0.52 (0.05)	0.21 (0.01)	6.62 (0.03)	0.73 (0.08)	0.99 (0.13)	10.53(0.17)	4.53(0.13)	0.90(0.09)
26	0	MLB10	168.18/-16.28	0.08 (0.01)	4.16 (0.21)	2.19 (0.55)	1.19 (0.36)	4.93(0.49)
26	1	MLB10	168.18/-16.28	0.55 (0.02)	6.61 (0.02)	1.25 (0.04)	1.10 (0.02)	6.54 (0.01)	1.20 (0.03)	8.69 (0.25)	12.47(0.12)	15.84(0.37)	4.93(0.49)
27	0	LDN1498	170.14/-19.11	0.40 (0.02)	8.01 (0.02)	0.79 (0.04)	0.88 (0.03)	7.99 (0.01)	0.71 (0.02)	4.10 (0.18)	9.34(0.11)	6.19(0.23)	1.56(0.16)

Table 2 continued

Table 2 (continued)

Srcid	Comp	Name	gl/gb	OH 1665 MHz			OH 1667 MHz				T_k	$N(^{13}\text{CO})$	$N(\text{H}_2)$
				T_{peak}	V_{cen}	ΔV	T_{peak}	V_{cen}	ΔV	$N(\text{OH})$			
				K	km s ⁻¹	km s ⁻¹	K	km s ⁻¹	km s ⁻¹	10 ¹⁴ cm ⁻²			
28	0	LM16	170.87/-15.87	0.40 (0.02)	6.33 (0.02)	1.02 (0.05)	0.72 (0.03)	6.30 (0.02)	1.06 (0.05)	5.12 (0.34)	9.44(0.10)	13.34(0.77)	2.41(0.24)
29	0	LM53	171.36/-10.72	0.31 (0.02)	5.80 (0.05)	2.32 (0.13)	5.01 (0.42)	6.03(0.13)	1.18(0.09)	2.05(0.20)
29	1	LM53	171.36/-10.72	0.78 (0.03)	5.94 (0.01)	0.55 (0.02)	1.11 (0.03)	5.95 (0.01)	0.38 (0.01)	2.91 (0.14)	5.08(0.30)	0.00(0.00)	2.05(0.20)
30	0	LDN1508	171.62/-11.36	0.34 (0.01)	5.53 (0.03)	1.38 (0.07)	0.46 (0.01)	5.48 (0.02)	1.53 (0.05)	4.89 (0.23)	8.65(0.07)	2.57(0.11)	2.14(0.21)
31	0	MLB16	171.80/-15.42	0.40 (0.02)	6.33 (0.02)	1.02 (0.05)	0.72 (0.03)	6.30 (0.02)	1.06 (0.05)	5.20 (0.35)	9.44(0.10)	13.34(0.77)	2.46(0.25)
32	0	B222	172.79/-5.11	0.06 (0.02)	-6.06 (0.11)	0.68 (0.26)	0.09 (0.02)	-5.93 (0.10)	1.10 (0.25)	0.72 (0.21)	5.48(0.10)	1.02(0.23)	0.60(0.06)
32	1	B222	172.79/-5.11	0.22 (0.02)	7.10 (0.03)	0.49 (0.06)	0.44 (0.03)	7.08 (0.01)	0.45 (0.03)	1.40 (0.14)	13.03(0.11)	4.78(0.10)	0.60(0.06)
32	2	B222	172.79/-5.11	0.18 (0.02)	13.45 (0.05)	1.21 (0.13)	1.59 (0.23)	0.60(0.06)
33	0	LDN1525	173.30/3.22	0.06 (0.01)	-22.66 (0.26)	3.66 (0.64)	1.66 (0.38)	1.59(0.16)
33	1	LDN1525	173.30/3.22	0.10 (0.02)	-5.96 (0.10)	1.27 (0.23)	0.14 (0.02)	-5.91 (0.06)	1.13 (0.15)	1.16 (0.21)	9.50(0.08)	3.25(0.11)	1.59(0.16)
33	2	LDN1525	173.30/3.22	0.16 (0.02)	10.51 (0.04)	0.70 (0.11)	0.82 (0.16)	1.59(0.16)
34	0	G171.84-05.22	171.848/-5.230	2.56 (0.17)	7.03 (0.01)	0.38 (0.03)	4.31 (0.23)	7.05 (0.01)	0.37 (0.02)	11.52 (0.98)	11.82(0.35)	9.86(1.06)	4.01(0.80)
35	0	G173.45-05.43	173.452/-5.436	0.84 (0.27)	6.75 (0.07)	0.30 (0.12)	1.54 (0.11)	6.73 (0.02)	0.42 (0.03)	4.64 (0.48)	13.57(0.28)	5.78(0.25)	1.40(0.57)
36	0	G173.78-05.26	173.782/-5.267	0.75 (0.12)	7.51 (0.04)	0.44 (0.07)	2.34 (0.53)	11.06(0.15)	3.14(0.10)	1.04(0.55)
37	0	G175.16-16.74	175.166/-16.744	2.19 (0.08)	5.77 (0.02)	0.84 (0.04)	3.94 (0.10)	5.88 (0.01)	0.80 (0.02)	21.46 (0.84)	7.95(0.90)	15.55(13.91)	2.00(1.56)
38	0	G175.58-16.60	175.583/-16.607	2.08 (0.10)	5.75 (0.02)	0.78 (0.04)	3.57 (0.10)	5.74 (0.01)	0.77 (0.03)	18.54 (0.80)	10.21(0.21)	12.78(0.75)	2.93(1.23)
39	0	G176.17-02.10	176.177/-2.108	2.06 (0.09)	-20.48 (0.02)	0.85 (0.04)	3.33 (0.10)	-20.49 (0.01)	0.74 (0.03)	17.98 (0.81)	10.26(0.19)	6.21(0.31)	2.01(0.80)
40	0	G176.35+01.92	176.352/1.921	0.66 (0.05)	-9.50 (0.08)	1.97 (0.19)	1.10 (0.06)	-9.48 (0.04)	1.66 (0.10)	12.67 (1.03)	8.11(0.16)	8.87(0.39)	1.19(0.34)
41	0	G176.37-02.05	176.374/-2.052	1.27 (0.08)	-20.37 (0.03)	1.08 (0.08)	2.43 (0.07)	-20.21 (0.01)	0.97 (0.03)	17.28 (0.79)	11.08(0.16)	9.53(0.42)	1.50(0.77)
42	0	G177.09+02.85	177.100/2.855	0.52 (0.05)	-10.12 (0.13)	2.68 (0.31)	0.69 (0.05)	-10.27 (0.08)	2.07 (0.19)	9.93 (1.21)	7.71(0.11)	4.77(0.26)	1.73(0.45)
43	0	G177.14-01.21	177.143/-1.213	1.14 (0.06)	-16.96 (0.04)	1.78 (0.10)	2.12 (0.06)	-17.03 (0.02)	1.65 (0.06)	25.10 (1.11)	12.43(0.13)	24.81(0.57)	2.52(0.66)
44	0	G177.869/1.044	177.869/1.044	0.60 (0.05)	-18.14 (0.10)	2.28 (0.23)	0.92 (0.06)	-18.13 (0.05)	1.58 (0.12)	10.20 (1.00)	8.45(0.44)	10.09(0.39)	1.28(0.30)
45	0	G178.28-00.61	178.286/-0.616	1.23 (0.11)	-0.79 (0.08)	1.09 (0.16)	2.19 (0.07)	-0.79 (0.03)	1.20 (0.07)	18.60 (1.21)	10.85(0.19)	8.53(0.41)	2.72(0.64)
45	1	G178.28-00.61	178.286/-0.616	0.71 (0.09)	0.75 (0.15)	1.45 (0.35)	1.39 (0.07)	0.86 (0.04)	1.24 (0.11)	12.18 (1.24)	11.88(0.18)	8.23(0.38)	2.72(0.64)
46	0	G178.48-06.76	178.484/-6.767	2.07 (0.07)	7.23 (0.02)	1.24 (0.05)	3.55 (0.10)	7.18 (0.02)	1.10 (0.04)	28.03 (1.24)	13.47(0.35)	17.12(1.03)	2.55(1.18)
47	0	G179.14-06.27	179.143/-6.279	2.04 (0.11)	7.77 (0.02)	0.63 (0.04)	2.95 (0.11)	7.79 (0.01)	0.62 (0.03)	13.26 (0.72)	8.54(0.30)	0.00(0.00)	1.44(0.63)
48	0	G179.29+04.20	179.297/4.200	1.11 (0.06)	1.15 (0.04)	1.66 (0.10)	1.86 (0.06)	1.09 (0.03)	1.80 (0.06)	23.00 (1.06)	9.51(0.21)	13.27(0.97)	2.89(1.01)
49	0	G181.16+04.33	181.164/4.331	0.32 (0.03)	1.78 (0.08)	1.71 (0.19)	0.56 (0.03)	1.92 (0.06)	2.07 (0.14)	8.03 (0.70)	10.65(0.20)	15.90(0.73)	2.65(2.87)
50	0	G181.71+04.16	181.714/4.163	0.51 (0.03)	3.36 (0.05)	1.70 (0.12)	0.89 (0.04)	3.34 (0.04)	2.02 (0.10)	12.42 (0.81)	10.56(0.18)	10.74(0.51)	1.95(1.44)
50	1	G181.71+04.16	181.714/4.163	0.17 (0.05)	-6.18 (0.16)	1.15 (0.38)	1.38 (0.61)	1.95(1.44)
51	0	G181.88+04.49	181.890/4.499	0.64 (0.03)	5.30 (0.03)	1.20 (0.07)	1.15 (0.05)	5.09 (0.03)	1.51 (0.07)	11.93 (0.75)	7.47(0.15)	6.10(0.37)	1.61(1.31)
52	0	G191.51-00.76	191.514/-0.765	2.04 (0.08)	-0.05 (0.02)	1.13 (0.05)	3.49 (0.08)	-0.06 (0.01)	1.01 (0.03)	25.86 (0.98)	13.67(0.26)	18.47(0.81)	3.05(1.33)
52	1	G191.51-00.76	191.514/-0.765	0.42 (0.12)	3.23 (0.07)	0.51 (0.15)	0.20 (0.03)	4.68 (0.82)	12.67 (2.01)	18.34 (3.74)	3.05(1.33)
53	0	G201.13+00.31	201.138/0.317	1.80 (0.07)	5.19 (0.02)	0.94 (0.04)	3.03 (0.07)	5.17 (0.01)	0.97 (0.03)	20.79 (0.76)	11.10(0.19)	12.44(0.54)	2.56(0.26)
54	0	G201.26+00.46	201.269/0.466	1.10 (0.06)	5.31 (0.05)	1.72 (0.12)	1.90 (0.06)	5.30 (0.03)	1.97 (0.07)	26.69 (1.26)	11.17(0.14)	16.48(0.53)	1.37(1.56)
55	0	G201.84+02.81	201.841/2.817	0.73 (0.06)	5.90 (0.04)	0.93 (0.09)	1.22 (0.05)	5.89 (0.02)	1.12 (0.06)	9.59 (0.65)	13.63(0.15)	11.58(0.39)	0.97(0.52)
55	1	G201.84+02.81	201.841/2.817	0.30 (0.05)	8.78 (0.11)	1.41 (0.27)	2.91 (0.73)	0.97(0.52)
56	0	G158.40-21.86	158.401/-21.864	0.92 (0.05)	4.33 (0.03)	1.08 (0.06)	1.78 (0.05)	4.25 (0.01)	0.88 (0.03)	10.38 (0.45)	11.98(0.16)	16.29(0.57)	7.08(4.11)
57	0	G158.86-21.60	158.862/-21.603	0.90 (0.05)	4.89 (0.03)	0.97 (0.06)	1.36 (0.05)	4.92 (0.02)	1.07 (0.04)	9.71 (0.52)	14.84(0.18)	16.11(0.82)	5.06(3.48)
59	0	G159.78-24.80	159.785/-24.809	0.28 (0.07)	2.71 (0.05)	0.42 (0.11)	0.23 (0.07)	3.46 (0.06)	0.39 (0.15)	0.60 (0.30)	10.42(0.29)	3.61(0.50)	0.29(0.08)
60	0	G168.00-15.69	168.003/-15.695	1.40 (0.06)	7.75 (0.01)	0.59 (0.03)	2.43 (0.06)	7.77 (0.01)	0.62 (0.02)	10.07 (0.38)	13.80(0.32)	15.56(0.62)	2.96(1.11)
61	0	G168.13-16.39	168.135/-16.393	2.13 (0.07)	6.43 (0.01)	0.64 (0.02)	4.01 (0.08)	6.44 (0.01)	0.60 (0.01)	15.98 (0.48)	11.70(0.28)	17.20(1.02)	18.44(15.94)
62	0	G168.72-15.48	168.728/-15.482	0.48 (0.04)	6.07 (0.05)	1.12 (0.14)	3.63 (0.56)	6.21(1.83)
62	1	G168.72-15.48	168.728/-15.482	2.51 (0.06)	7.30 (0.01)	0.57 (0.02)	4.03 (0.06)	7.33 (0.00)	0.57 (0.01)	15.53 (0.38)	12.93(0.25)	21.76(2.51)	6.21(1.83)
63	0	G169.82-19.39	169.827/-19.392	0.95 (0.06)	8.08 (0.02)	0.62 (0.04)	2.41 (0.06)	8.13 (0.01)	0.48 (0.01)	7.59 (0.31)	13.45(0.17)	11.08(0.52)	3.49(2.03)
64	0	G169.84-07.61	169.849/-7.613	0.86 (0.07)	6.43 (0.02)	0.44 (0.04)	1.50 (0.07)	6.38 (0.01)	0.47 (0.03)	5.06 (0.38)	10.92(0.11)	5.87(0.19)	2.07(0.45)
65	0	G170.77-08.51	170.771/-8.518	0.92 (0.07)	6.83 (0.02)	0.41 (0.04)	1.17 (0.07)	6.79 (0.02)	0.59 (0.04)	4.83 (0.44)	12.16(0.28)	8.11(0.49)	1.65(0.40)

Table 2 continued

Table 2 (continued)

Srcid	Comp	Name	gl/gb	OH 1665 MHz			OH 1667 MHz				T_k	$N(^{13}\text{CO})$	$N(\text{H}_2)$
				T_{peak}	V_{cen}	ΔV	T_{peak}	V_{cen}	ΔV	$N(\text{OH})$			
				K	km s^{-1}	km s^{-1}	K	km s^{-1}	km s^{-1}	10^{14} cm^{-2}			
66	0	G170.88-10.92	170.881/-10.921	0.86 (0.07)	5.98 (0.02)	0.49 (0.04)	1.67 (0.08)	5.99 (0.01)	0.36 (0.02)	4.18 (0.30)	8.74(0.16)	10.66(1.42)	4.06(1.34)
67	0	G171.34-10.67	171.343/-10.674	1.24 (0.06)	6.26 (0.02)	0.68 (0.04)	1.87 (0.06)	6.29 (0.01)	0.69 (0.03)	8.96 (0.44)	7.87(0.43)	0.00(0.00)	6.16(1.46)
68	0	G173.07-16.52	173.079/-16.529	1.35 (0.06)	6.69 (0.01)	0.56 (0.03)	2.34 (0.07)	6.71 (0.01)	0.51 (0.02)	8.10 (0.34)	14.41(0.29)	14.00(0.84)	3.51(2.23)
69	0	G173.07-17.89	173.079/-17.896	0.51 (0.04)	3.91 (0.05)	1.05 (0.11)	0.75 (0.06)	4.06 (0.03)	0.74 (0.06)	3.77 (0.42)	12.89(0.18)	12.60(0.46)	2.48(0.55)
70	0	G173.12-13.32	173.122/-13.325	1.23 (0.06)	5.41 (0.02)	0.62 (0.04)	2.01 (0.06)	5.37 (0.01)	0.65 (0.02)	9.01 (0.41)	8.66(1.20)	0.00(0.00)	1.83(0.86)
70	1	G173.12-13.32	173.122/-13.325	0.50 (0.05)	6.50 (0.06)	0.99 (0.15)	7.21(0.45)	4.29(1.26)	1.83(0.86)
71	0	G173.36-16.27	173.364/-16.277	1.85 (0.06)	6.35 (0.01)	0.54 (0.02)	3.17 (0.07)	6.35 (0.01)	0.59 (0.01)	12.62 (0.40)	12.22(0.40)	17.90(2.72)	6.89(1.26)
72	0	G173.69-15.55	173.694/-15.559	1.06 (0.05)	6.30 (0.02)	0.67 (0.04)	1.72 (0.06)	6.28 (0.01)	0.63 (0.02)	7.31 (0.38)	11.10(0.31)	9.21(0.81)	6.26(2.85)
73	0	G173.91-16.25	173.913/-16.257	0.83 (0.05)	6.09 (0.03)	0.86 (0.06)	1.87 (0.06)	6.17 (0.01)	0.65 (0.02)	8.18 (0.41)	15.35(0.34)	14.96(0.90)	3.29(2.13)
74	0	G173.95-13.74	173.957/-13.747	2.17 (0.05)	6.31 (0.01)	1.08 (0.03)	2.66 (0.05)	6.25 (0.01)	1.27 (0.03)	23.03 (0.65)	12.97(0.28)	32.77(2.57)	6.39(2.50)
75	0	G174.06-15.81	174.067/-15.811	1.61 (0.05)	6.23 (0.01)	0.86 (0.03)	2.52 (0.05)	6.26 (0.01)	0.86 (0.02)	14.70 (0.48)	13.40(0.17)	25.98(1.00)	8.44(2.14)
76	0	G174.39-13.43	174.397/-13.440	1.88 (0.05)	5.81 (0.01)	1.19 (0.03)	3.19 (0.06)	5.75 (0.01)	0.94 (0.02)	20.71 (0.55)	11.79(0.27)	21.47(0.91)	18.68(17.11)
77	0	G174.44-15.75	174.441/-15.753	0.80 (0.06)	5.27 (0.02)	0.58 (0.05)	1.04 (0.05)	5.23 (0.02)	0.81 (0.05)	5.68 (0.47)	7.98(0.29)	2.94(0.56)	1.69(1.46)
77	1	G174.44-15.75	174.441/-15.753	0.72 (0.05)	6.88 (0.03)	0.86 (0.07)	1.00 (0.05)	6.80 (0.02)	0.98 (0.06)	6.62 (0.52)	13.77(0.23)	18.82(1.41)	1.69(1.46)
78	0	G174.50-19.88	174.507/-19.887	0.37 (0.05)	7.75 (0.07)	0.93 (0.16)	2.32 (0.51)	9.64(0.27)	10.61(1.69)	1.00(0.36)
79	0	G174.57-13.66	174.573/-13.670	1.53 (0.08)	5.37 (0.01)	0.39 (0.02)	2.39 (0.08)	5.37 (0.01)	0.36 (0.02)	5.95 (0.32)	11.53(0.49)	13.42(3.45)	2.42(2.42)
79	1	G174.57-13.66	174.573/-13.670	1.45 (0.05)	6.27 (0.02)	0.85 (0.04)	1.67 (0.05)	6.26 (0.01)	0.89 (0.04)	10.19 (0.53)	9.69(0.93)	9.55(1.62)	2.42(2.42)
80	0	G174.70-15.48	174.704/-15.482	1.46 (0.05)	5.83 (0.02)	0.88 (0.04)	2.41 (0.06)	5.85 (0.01)	0.82 (0.02)	13.22 (0.47)	14.05(0.23)	22.63(1.11)	12.01(3.26)
81	0	G174.81-15.15	174.814/-15.153	1.35 (0.06)	5.69 (0.01)	0.58 (0.03)	2.19 (0.07)	5.72 (0.01)	0.53 (0.02)	7.79 (0.37)	6.95(0.10)	0.00(0.00)	2.76(0.74)
82	0	G174.88-17.11	174.880/-17.114	0.43 (0.03)	5.84 (0.08)	2.05 (0.18)	0.66 (0.04)	5.92 (0.05)	1.77 (0.12)	7.91 (0.68)	11.30(0.26)	11.95(1.04)	2.96(0.97)
83	0	G175.31-20.50	175.320/-20.503	0.39 (0.08)	8.42 (0.04)	0.41 (0.10)	1.10 (0.34)	9.15(0.28)	5.50(0.69)	0.69(0.07)
84	0	G175.34-10.82	175.342/-10.826	0.78 (0.09)	5.62 (0.02)	0.29 (0.04)	0.97 (0.10)	5.54 (0.01)	0.30 (0.04)	2.04 (0.35)	7.71(0.37)	0.00(0.00)	0.72(0.18)
84	1	G175.34-10.82	175.342/-10.826	0.32 (0.06)	6.40 (0.07)	0.72 (0.17)	0.54 (0.04)	6.37 (0.07)	1.25 (0.17)	4.66 (0.74)	0.72(0.18)
85	0	G175.49-16.80	175.495/-16.802	1.91 (0.09)	5.56 (0.01)	0.29 (0.02)	3.16 (0.08)	5.55 (0.01)	0.42 (0.01)	8.98 (0.36)	9.61(0.18)	9.36(1.01)	5.31(1.75)
85	1	G175.49-16.80	175.495/-16.802	0.33 (0.04)	5.95 (0.11)	2.11 (0.25)	5.31(1.75)
86	0	G175.97-20.38	175.979/-20.384	0.42 (0.07)	7.50 (0.03)	0.39 (0.08)	1.13 (0.30)	8.96(0.23)	2.89(0.26)	0.47(0.13)
87	0	G176.52-09.80	176.528/-9.802	0.95 (0.06)	7.41 (0.02)	0.64 (0.05)	1.94 (0.06)	7.38 (0.01)	0.49 (0.02)	6.55 (0.33)	6.61(0.19)	0.00(0.00)	2.03(0.57)
88	0	G177.97-09.72	177.978/-9.727	2.49 (0.07)	7.15 (0.01)	0.47 (0.01)	3.96 (0.07)	7.15 (0.00)	0.45 (0.01)	12.52 (0.35)	14.85(0.26)	12.43(0.47)	8.86(1.58)
89	0	G178.72-07.01	178.725/-7.012	1.10 (0.06)	7.02 (0.01)	0.38 (0.02)	1.81 (0.06)	7.03 (0.01)	0.38 (0.02)	4.96 (0.27)	12.50(0.32)	8.39(0.64)	3.12(3.00)
90	0	G178.98-06.74	178.989/-6.749	1.52 (0.06)	7.75 (0.01)	0.66 (0.03)	2.43 (0.06)	7.72 (0.01)	0.63 (0.02)	11.00 (0.43)	11.70(0.27)	13.49(0.92)	6.68(1.73)
91	0	G181.42-03.73	181.428/-3.733	0.39 (0.04)	-5.39 (0.07)	1.41 (0.16)	4.09 (0.61)	11.60(0.16)	7.98(0.45)	3.16(0.67)
92	0	G181.84+00.31	181.846/0.317	0.30 (0.05)	-9.05 (0.11)	1.44 (0.26)	3.11 (0.73)	7.57(0.16)	1.89(0.43)	3.58(1.39)
92	1	G181.84+00.31	181.846/0.317	0.83 (0.05)	3.09 (0.04)	1.47 (0.09)	8.79 (0.74)	9.90(0.14)	10.23(0.44)	3.58(1.39)
93	0	G185.33-02.12	185.339/-2.127	0.40 (0.03)	-0.35 (0.10)	1.54 (0.22)	0.69 (0.07)	-0.32 (0.15)	1.64 (0.22)	8.34 (1.39)	7.52(0.32)	2.06(0.29)	2.21(0.91)
93	1	G185.33-02.12	185.339/-2.127	0.38 (0.03)	1.52 (0.11)	1.52 (0.26)	0.55 (0.06)	1.35 (0.18)	1.69 (0.34)	6.90 (1.55)	7.89(0.20)	9.34(0.61)	2.21(0.91)
93	2	G185.33-02.12	185.339/-2.127	0.19 (0.04)	3.75 (0.10)	1.05 (0.24)	0.23 (0.03)	3.92 (0.12)	1.57 (0.30)	2.68 (0.63)	2.21(0.91)
94	0	G192.12-10.90	192.129/-10.902	1.15 (0.06)	10.04 (0.02)	0.65 (0.04)	1.69 (0.06)	10.06 (0.01)	0.75 (0.03)	8.75 (0.45)	17.91(0.14)	18.54(0.41)	3.26(1.22)
95	0	G192.28-11.33	192.283/-11.339	0.98 (0.05)	10.16 (0.02)	1.08 (0.06)	1.52 (0.04)	10.06 (0.02)	1.25 (0.04)	13.21 (0.54)	16.76(0.26)	28.67(0.62)	1.48(1.13)
96	0	G198.03-15.24	198.039/-15.249	0.50 (0.07)	-0.08 (0.05)	0.66 (0.11)	0.78 (0.08)	-0.15 (0.03)	0.63 (0.07)	3.37 (0.51)	13.07(0.39)	9.79(0.40)	1.21(0.42)
98	0	G038.95-00.47	38.96/-0.47	-1.49 (0.03)	41.55 (0.04)	3.82 (0.09)	-0.79 (0.02)	41.78 (0.10)	7.24 (0.23)	70.05 (2.96)	20.22(0.13)	102.24(1.44)	53.90(5.39)
98	1	G038.95-00.47	38.96/-0.47	-0.16 (0.06)	61.30 (0.19)	1.09 (0.45)	2.05 (1.13)	7.86(0.11)	8.62(0.59)	53.90(5.39)
98	2	G038.95-00.47	38.96/-0.47	0.34 (0.02)	80.14 (0.20)	5.77 (0.48)	0.54 (0.03)	78.92 (0.19)	5.31 (0.47)	48.74 (4.94)	53.90(5.39)
98	3	G038.95-00.47	38.96/-0.47	0.24 (0.04)	83.97 (0.29)	3.02 (0.65)	12.47 (3.34)	6.05(0.13)	3.11(0.67)	53.90(5.39)
99	0	G043.02+08.36	43.02/8.37	0.28 (0.03)	4.00 (0.05)	0.87 (0.11)	0.36 (0.03)	4.04 (0.04)	1.09 (0.10)	3.33 (0.42)	11.55(0.17)	12.62(0.64)	5.77(1.69)
99	1	G043.02+08.36	43.02/8.37	0.17 (0.03)	8.32 (0.10)	1.19 (0.23)	5.77(1.69)
99	2	G043.02+08.36	43.02/8.37	0.16 (0.03)	12.62 (0.07)	0.72 (0.18)	5.77(1.69)
100	0	G046.75-07.68	46.76/-7.69	0.48 (0.06)	7.30 (0.03)	0.56 (0.07)	0.98 (0.07)	7.21 (0.02)	0.51 (0.04)	4.15 (0.43)	11.18(0.22)	4.89(0.24)	0.65(0.32)

Table 2 continued

Table 2 (continued)

Srcid	Comp	Name	gl/gb	OH 1665 MHz			OH 1667 MHz				T_k	$N(^{13}\text{CO})$	$N(\text{H}_2)$
				T_{peak}	V_{cen}	ΔV	T_{peak}	V_{cen}	ΔV	$N(\text{OH})$			
				K	km s $^{-1}$	km s $^{-1}$	K	km s $^{-1}$	km s $^{-1}$	10 14 cm $^{-2}$			
101	0	G047.74-05.56	47.75/-5.57	0.50 (0.06)	8.23 (0.03)	0.52 (0.07)	0.62 (0.06)	8.18 (0.03)	0.62 (0.07)	3.29 (0.48)	11.68(0.21)	5.17(0.29)	1.92(0.64)
102	0	G048.25-05.73	48.25/-5.74	1.14 (0.07)	9.01 (0.01)	0.43 (0.03)	1.70 (0.06)	9.01 (0.01)	0.52 (0.02)	7.38 (0.37)	11.61(0.25)	12.68(0.88)	3.97(1.25)
103	0	G048.40-05.82	48.41/-5.83	1.30 (0.07)	9.19 (0.01)	0.54 (0.03)	2.10 (0.06)	9.25 (0.01)	0.60 (0.02)	10.54 (0.48)	9.55(0.22)	8.31(0.69)	4.73(1.77)
104	0	G048.65-00.29	48.66/-0.29	-0.43 (0.06)	5.55 (0.06)	0.84 (0.13)	-0.50 (0.04)	5.60 (0.09)	2.53 (0.21)	10.73 (1.18)	26.80(2.68)
104	1	G048.65-00.29	48.66/-0.29	-0.53 (0.03)	33.11 (0.11)	4.56 (0.26)	-0.51 (0.02)	33.37 (0.14)	6.25 (0.33)	27.22 (1.88)	11.21(0.09)	23.54(0.58)	26.80(2.68)
105	0	G048.82-03.82	48.82/-3.83	0.32 (0.05)	9.31 (0.05)	0.57 (0.11)	1.57 (0.41)	10.58(0.23)	4.37(0.31)	0.41(0.20)
106	0	G049.06-04.18	49.06/-4.18	0.29 (0.04)	9.76 (0.11)	1.52 (0.26)	3.63 (0.81)	10.41(0.16)	5.14(0.28)	0.63(0.23)
107	0	G049.76-07.25	49.77/-7.26	0.52 (0.05)	21.31 (0.04)	0.85 (0.09)	0.91 (0.05)	21.26 (0.02)	0.81 (0.05)	5.90 (0.48)	8.53(0.21)	6.47(0.46)	0.46(0.05)
108	0	G052.99+03.07	53.00/3.08	0.25 (0.04)	6.98 (0.13)	1.50 (0.31)	3.21 (0.87)	4.20(0.27)	0.56(0.23)	2.21(0.52)
108	1	G052.99+03.07	53.00/3.08	0.50 (0.04)	10.33 (0.05)	1.33 (0.12)	0.64 (0.05)	10.26 (0.04)	1.12 (0.10)	6.16 (0.75)	9.97(0.18)	11.25(0.58)	2.21(0.52)
112	0	G054.03-02.38	54.03/-2.39	0.60 (0.05)	17.06 (0.03)	0.66 (0.07)	0.91 (0.05)	17.13 (0.02)	0.85 (0.05)	6.79 (0.57)	7.83(0.20)	4.98(0.45)	1.24(0.29)
113	0	G056.84+04.81	56.84/4.82	0.50 (0.04)	10.89 (0.05)	1.07 (0.11)	0.67 (0.04)	10.94 (0.04)	1.32 (0.09)	6.76 (0.64)	12.46(0.27)	9.13(0.43)	1.10(0.37)
114	0	G057.08+04.46	57.08/4.46	0.67 (0.05)	10.66 (0.03)	0.70 (0.07)	0.84 (0.05)	10.57 (0.03)	0.93 (0.06)	6.08 (0.55)	10.80(0.26)	7.13(0.31)	0.91(0.28)
115	0	G057.10+03.65	57.11/3.66	1.02 (0.04)	11.21 (0.03)	1.48 (0.06)	1.54 (0.04)	11.19 (0.02)	1.62 (0.04)	19.95 (0.71)	12.84(0.20)	26.54(1.00)	5.67(1.17)
116	0	G057.17+03.41	57.17/3.42	0.54 (0.04)	10.79 (0.05)	1.43 (0.12)	0.21 (0.03)	7.23 (0.17)	2.32 (0.40)	3.84 (0.87)	2.21(0.96)
116	1	G057.17+03.41	57.17/3.42	1.11 (0.04)	10.94 (0.02)	1.48 (0.06)	13.26 (0.69)	12.11(0.19)	13.80(0.52)	2.21(0.96)
117	0	G057.26+04.01	57.26/4.01	0.79 (0.05)	10.70 (0.03)	0.78 (0.06)	1.31 (0.05)	10.74 (0.02)	0.77 (0.04)	7.94 (0.50)	12.33(0.17)	8.39(0.38)	2.07(1.09)
118	0	G058.02+03.02	58.03/3.02	1.11 (0.05)	9.78 (0.02)	0.88 (0.04)	1.62 (0.06)	9.83 (0.01)	0.70 (0.03)	9.27 (0.50)	9.77(0.17)	7.17(0.45)	2.87(0.94)
119	0	G058.07+03.20	58.07/3.21	0.89 (0.04)	9.83 (0.03)	1.17 (0.07)	1.61 (0.05)	9.81 (0.01)	0.96 (0.03)	12.47 (0.59)	7.40(0.15)	9.38(1.00)	2.23(1.08)
120	0	G058.16+03.50	58.16/3.51	0.46 (0.03)	10.44 (0.07)	1.85 (0.16)	0.63 (0.03)	10.45 (0.05)	2.04 (0.13)	10.28 (0.84)	8.71(0.19)	11.63(0.55)	6.26(1.19)
121	0	G058.97-01.66	58.97/-1.66	0.21 (0.04)	8.42 (0.13)	1.35 (0.32)	0.22 (0.02)	9.58 (0.18)	3.74 (0.43)	6.83 (1.03)	7.27(0.18)	1.57(0.28)	1.69(0.75)
121	1	G058.97-01.66	58.97/-1.66	0.46 (0.03)	23.09 (0.05)	1.49 (0.12)	5.84 (0.64)	14.01(0.15)	15.49(0.67)	1.69(0.75)
122	0	G060.75-01.23	60.75/-1.23	0.30 (0.03)	11.26 (0.11)	2.15 (0.26)	0.63 (0.03)	11.32 (0.05)	2.13 (0.12)	12.14 (0.87)	10.30(0.18)	23.02(1.89)	2.79(1.49)
123	0	G061.76-10.80	61.77/-10.81	0.41 (0.05)	12.08 (0.05)	0.98 (0.13)	2.81 (0.48)	9.04(0.23)	3.08(0.46)	0.27(0.07)
124	0	G065.43-03.15	65.43/-3.15	0.85 (0.04)	5.91 (0.03)	1.39 (0.08)	0.95 (0.04)	5.96 (0.02)	1.09 (0.06)	8.42 (0.59)	7.49(0.14)	8.69(0.55)	2.23(0.64)
125	0	G070.44-01.54	70.44/-1.55	0.49 (0.03)	10.84 (0.06)	1.65 (0.13)	1.03 (0.03)	10.88 (0.04)	2.92 (0.09)	26.72 (1.14)	16.42(0.12)	45.20(0.69)	7.44(2.01)
126	0	G070.72-00.63	70.73/-0.63	0.44 (0.03)	10.40 (0.17)	3.01 (0.41)	0.82 (0.02)	10.21 (0.12)	4.51 (0.27)	32.90 (2.17)	12.58(0.24)	23.94(2.83)	13.70(7.08)
126	1	G070.72-00.63	70.73/-0.63	0.38 (0.06)	12.90 (0.10)	1.34 (0.25)	0.76 (0.06)	13.26 (0.04)	1.54 (0.13)	10.42 (1.20)	10.95(0.52)	16.08(2.17)	13.70(7.08)
127	0	G037.49+03.03	37.49/3.03	0.31 (0.03)	15.86 (0.05)	1.06 (0.12)	0.97 (0.03)	15.47 (0.02)	0.95 (0.04)	9.92 (0.53)	9.12(0.14)	10.52(0.47)	1.48(0.70)
129	0	G062.16-02.92	62.17/-2.93	0.38 (0.03)	13.05 (0.08)	2.12 (0.19)	0.73 (0.04)	12.47 (0.03)	1.20 (0.08)	6.96 (0.59)	7.99(0.11)	2.49(0.13)	0.53(0.30)
130	0	G069.57-01.74	69.71/-1.70	0.25 (0.04)	14.41 (0.10)	1.41 (0.26)	3.13 (0.76)	7.23(0.25)	2.64(0.24)	5.49(0.55)
132	0	SDC033.107-0.065	33.107/-0.065	-1.02 (1.04)	10.61 (1.02)	2.04 (2.43)	-1.53 (0.14)	10.29 (0.09)	1.87 (0.20)	37.15 (5.36)	7.29(0.64)	2.82(0.68)	-0.00(-0.00)
133	0	SDC033.332-0.531	33.332/-0.531	-0.27 (0.03)	94.69 (0.21)	4.40 (0.50)	0.29 (0.03)	91.39 (0.17)	3.29 (0.40)	15.42 (2.47)	13.48(0.15)	39.56(0.82)	-0.00(-0.00)
134	0	SDC033.382+0.204	33.382/+0.204	-0.69 (0.02)	11.66 (0.12)	6.66 (0.28)	-0.89 (0.03)	11.62 (0.09)	6.46 (0.21)	74.89 (3.26)	8.16(0.12)	4.07(0.47)	-0.00(-0.00)
134	1	SDC033.382+0.204	33.382/+0.204	-0.33 (0.04)	55.94 (0.17)	3.09 (0.39)	13.33 (2.24)	6.18(0.16)	1.21(0.29)	-0.00(-0.00)
135	0	SDC033.568+0.027	33.568/+0.027	-0.34 (0.04)	9.59 (0.25)	3.74 (0.63)	-0.50 (0.04)	9.90 (0.25)	5.26 (0.42)	34.90 (3.98)	-0.00(-0.00)
135	1	SDC033.568+0.027	33.568/+0.027	-0.86 (0.08)	12.18 (0.04)	0.89 (0.11)	-0.96 (0.08)	11.73 (0.04)	1.28 (0.13)	16.27 (2.07)	4.71(0.41)	2.08(0.39)	-0.00(-0.00)
135	2	SDC033.568+0.027	33.568/+0.027	-0.26 (0.04)	54.92 (0.25)	3.65 (0.61)	12.69 (2.77)	-0.00(-0.00)
135	3	SDC033.568+0.027	33.568/+0.027	0.28 (0.04)	71.95 (0.20)	2.54 (0.47)	12.82 (3.15)	9.35(0.10)	11.76(0.46)	-0.00(-0.00)
135	4	SDC033.568+0.027	33.568/+0.027	-0.27 (0.03)	106.98 (0.27)	4.90 (0.64)	-0.45 (0.04)	102.42 (0.12)	2.64 (0.30)	15.86 (2.35)	12.13(0.08)	15.64(1.02)	-0.00(-0.00)
136	0	SDC033.622-0.032	33.622/-0.032	-0.49 (0.04)	11.05 (0.14)	3.93 (0.34)	-1.11 (0.04)	10.96 (0.05)	2.88 (0.13)	42.19 (2.49)	8.00(0.16)	5.01(0.34)	-0.00(-0.00)
136	1	SDC033.622-0.032	33.622/-0.032	0.42 (0.05)	34.20 (0.11)	1.77 (0.27)	13.45 (2.66)	11.18(0.15)	20.63(0.62)	-0.00(-0.00)
136	2	SDC033.622-0.032	33.622/-0.032	-0.90 (0.03)	107.98 (0.09)	5.44 (0.22)	14.09(0.11)	62.14(1.58)	-0.00(-0.00)
137	0	SDC033.708+0.206	33.708/+0.206	-0.39 (0.05)	12.45 (0.08)	1.14 (0.18)	-0.28 (0.04)	11.97 (0.14)	1.87 (0.33)	7.02 (1.64)	7.50(0.46)	1.23(0.59)	-0.00(-0.00)
137	1	SDC033.708+0.206	33.708/+0.206	-0.40 (0.05)	56.88 (0.08)	1.52 (0.20)	-0.83 (0.03)	56.58 (0.07)	3.77 (0.16)	41.30 (2.33)	10.43(0.45)	12.93(1.01)	-0.00(-0.00)
138	0	SDC033.743-0.009	33.743/-0.009	-0.52 (0.06)	11.84 (0.09)	1.77 (0.22)	-1.04 (0.05)	11.37 (0.06)	2.63 (0.14)	36.45 (2.49)	7.19(0.55)	2.39(0.87)	-0.00(-0.00)
138	1	SDC033.743-0.009	33.743/-0.009	-0.56 (0.05)	56.37 (0.10)	2.18 (0.23)	16.40 (2.27)	5.46(0.46)	1.16(0.45)	-0.00(-0.00)

OH SURVEY TOWARD DARK CLOUDS

Table 2 continued

Table 2 (continued)

Srcid	Comp	Name	gl/gb	OH 1665 MHz			OH 1667 MHz				T_{k}	$N(^{13}\text{CO})$	$N(\text{H}_2)$
				T_{peak}	V_{cen}	ΔV	T_{peak}	V_{cen}	ΔV	$N(\text{OH})$			
				K	km s^{-1}	km s^{-1}	K	km s^{-1}	km s^{-1}	10^{14} cm^{-2}			
138	2	SDC033.743-0.009	33.743/-0.009	-0.66 (0.03)	110.15 (0.14)	6.14 (0.33)	-0.81 (0.03)	106.26 (0.12)	7.06 (0.29)	76.20 (4.12)	13.74(0.36)	42.48(2.84)	-0.00(-0.00)
139	0	SDC033.819-0.217	33.819/-0.217	-0.55 (0.03)	10.91 (0.12)	4.50 (0.28)	33.54 (2.79)	9.05(0.50)	11.39(1.36)	-0.00(-0.00)
140	0	SDC034.056-0.331	34.056/-0.331	-0.33 (0.05)	12.62 (0.10)	1.45 (0.24)	6.36 (1.40)	9.77(0.27)	17.33(0.91)	-0.00(-0.00)
141	0	SDC034.685-0.729	34.685/-0.729	-0.33 (0.05)	12.41 (0.13)	1.95 (0.32)	-0.84 (0.05)	12.07 (0.05)	1.78 (0.12)	18.26 (1.59)	9.03(0.12)	10.13(0.54)	-0.00(-0.00)
141	1	SDC034.685-0.729	34.685/-0.729	-0.72 (0.03)	44.90 (0.19)	9.04 (0.34)	-0.86 (0.03)	42.23 (0.12)	6.51 (0.32)	68.27 (3.90)	7.20(0.16)	8.49(0.81)	-0.00(-0.00)
141	2	SDC034.685-0.729	34.685/-0.729	-0.28 (0.05)	47.50 (0.18)	2.04 (0.49)	-0.27 (0.06)	47.00 (0.15)	1.68 (0.43)	5.58 (1.83)	15.63(0.13)	10.54(0.65)	-0.00(-0.00)
141	3	SDC034.685-0.729	34.685/-0.729	1.00 (0.05)	76.01 (0.04)	1.59 (0.10)	0.52 (0.05)	73.94 (0.08)	1.60 (0.18)	14.24 (2.10)	-0.00(-0.00)

Table 3. Gaussian fitting parameters of HINSA data.

Srcid	Name	gl/gb	N(OH)	N(HINSA)	p	Density	$N(\text{H}_2)$
			10^{14}cm^{-2}	10^{18}cm^{-2}		10^3cm^{-3}	10^{21}cm^{-2}
2	LDN621	35.35/2.34	4.24(0.49)	1.63(0.55)	0.81	...	4.70(0.47)
4	CB191	37.56/-6.15	2.01(0.33)	0.38(0.13)	0.68	...	0.37(0.04)
11	LDN649	43.03/-0.67	9.71(1.65)	3.20(1.83)	0.68	...	12.50(1.25)
12	IREC58	43.22/8.33	1.26(0.35)	4.24(2.15)	0.79	...	1.07(0.11)
12	IREC58	43.22/8.33	1.46(0.26)	0.93(0.36)	0.72	...	1.07(0.11)
14	LDN658	44.38/-2.33	1.68(0.33)	9.19(1.19)	0.63	...	1.39(0.14)
20	LDN666	45.25/9.11	5.65(0.47)	10.10(1.58)	0.69	...	1.96(0.20)
20	LDN666	45.25/9.11	1.92(0.30)	9.23(1.70)	0.61	...	1.96(0.20)
26	MLB10	168.18/-16.28	8.69(0.25)	9.16(2.64)	0.90	...	4.93(0.49)
29	LM53	171.36/-10.72	2.91(0.14)	0.74(0.24)	0.90	...	2.05(0.20)
33	LDN1525	173.3/3.22	1.16(0.21)	2.33(0.51)	0.38	...	1.59(0.16)
34	G171.84-05.22	171.848/-5.23	11.50(0.98)	1.37(0.74)	0.84	4.21(0.93)	4.01(0.80)
37	G175.16-16.74	175.166/-16.744	21.50(0.84)	1.16(0.56)	0.58	2.00(1.58)	2.00(1.56)
38	G175.58-16.60	175.583/-16.607	18.50(0.80)	2.69(0.96)	0.58	3.18(1.45)	2.93(1.23)
39	G176.17-02.10	176.177/-2.108	18.00(0.81)	3.16(2.08)	0.56	0.29(0.13)	2.01(0.80)
40	G176.35+01.92	176.352/1.921	12.70(1.03)	0.47(0.21)	0.90	...	1.19(0.34)
41	G176.37-02.05	176.374/-2.052	17.30(0.79)	4.96(2.59)	0.56	0.22(0.12)	1.50(0.77)
45	G178.28-00.61	178.286/-0.616	18.60(1.21)	2.50(1.05)	0.72	...	2.72(0.64)
45	G178.28-00.61	178.286/-0.616	12.20(1.24)	1.40(0.63)	0.72	...	2.72(0.64)
46	G178.48-06.76	178.484/-6.767	28.00(1.24)	2.67(1.45)	0.80	2.16(1.08)	2.55(1.18)
47	G179.14-06.27	179.143/-6.279	13.30(0.72)	1.89(0.96)	0.81	1.61(0.89)	1.44(0.63)
48	G179.29+04.20	179.297/4.2	23.00(1.06)	2.58(0.92)	0.90	...	2.89(1.01)
50	G181.71+04.16	181.714/4.163	12.40(0.81)	1.07(0.38)	0.90	...	1.95(1.44)
52	G191.51-00.76	191.514/-0.765	25.90(0.98)	2.73(1.36)	0.97	...	3.05(1.33)
53	G201.13+00.31	201.138/0.317	20.80(0.77)	2.05(1.33)	0.83	...	2.56(0.26)
54	G201.26+00.46	201.269/0.466	26.70(1.26)	1.16(0.34)	0.83	...	1.37(1.56)
55	G201.84+02.81	201.841/2.817	9.59(0.65)	5.67(2.54)	0.73	...	0.97(0.52)
56	G158.40-21.86	158.401/-21.864	10.40(0.45)	2.30(1.19)	0.64	10.95(6.51)	7.08(4.11)
57	G158.86-21.60	158.862/-21.603	9.71(0.52)	4.04(1.88)	0.64	9.07(6.37)	5.06(3.48)
60	G168.00-15.69	168.003/-15.695	10.10(0.38)	6.52(5.18)	0.73	4.89(1.93)	2.96(1.11)
62	G168.72-15.48	168.728/-15.482	15.50(0.38)	7.39(3.93)	0.73	11.53(3.70)	6.21(1.83)
64	G169.84-07.61	169.849/-7.613	5.06(0.38)	1.82(0.96)	0.85	3.78(0.93)	2.07(0.45)
65	G170.77-08.51	170.771/-8.518	4.83(0.44)	2.61(1.88)	0.76	1.58(0.41)	1.65(0.40)
67	G171.34-10.67	171.343/-10.674	8.96(0.44)	1.61(0.72)	0.71	7.09(1.82)	6.16(1.46)
68	G173.07-16.52	173.079/-16.529	8.10(0.34)	12.70(9.19)	0.58	3.90(2.52)	3.51(2.23)
70	G173.12-13.32	173.122/-13.325	9.01(0.41)	2.24(0.75)	0.65	2.00(0.96)	1.83(0.86)
71	G173.36-16.27	173.364/-16.277	12.60(0.40)	5.65(3.09)	0.59	10.03(2.12)	6.89(1.26)

Table 3 *continued*

Table 3 (continued)

Srcid	Name	gl/gb	N(OH)	N(HINSA)	p	Density	$N(\text{H}_2)$
			10^{14}cm^{-2}	10^{18}cm^{-2}		10^3cm^{-3}	10^{21}cm^{-2}
72	G173.69-15.55	173.694/-15.559	7.31(0.38)	2.14(1.07)	0.60	6.68(3.11)	6.26(2.85)
74	G173.95-13.74	173.957/-13.747	23.00(0.65)	14.80(8.98)	0.64	7.56(3.07)	6.39(2.50)
76	G174.39-13.43	174.397/-13.44	20.70(0.55)	7.12(3.81)	0.65	18.50(17.05)	18.68(17.11)
78	G174.50-19.88	174.507/-19.887	2.32(0.51)	1.64(1.18)	0.52	1.04(0.39)	1.00(0.36)
79	G174.57-13.66	174.573/-13.67	5.95(0.32)	1.89(0.77)	0.64	2.22(2.24)	2.42(2.42)
79	G174.57-13.66	174.573/-13.67	10.20(0.53)	4.07(1.95)	0.64	2.22(2.24)	2.42(2.42)
80	G174.70-15.48	174.704/-15.482	13.20(0.47)	6.55(4.65)	0.60	13.17(3.80)	12.01(3.26)
81	G174.81-15.15	174.814/-15.153	7.79(0.37)	0.71(0.33)	0.61	3.22(0.92)	2.76(0.74)
83	G175.31-20.50	175.32/-20.503	1.10(0.34)	0.37(0.07)	0.90	...	0.69(0.07)
85	G175.49-16.80	175.495/-16.802	8.98(0.35)	1.33(0.60)	0.58	6.01(2.07)	5.31(1.75)
87	G176.52-09.80	176.528/-9.802	6.55(0.33)	2.63(1.71)	0.90	...	2.03(0.57)
88	G177.97-09.72	177.978/-9.727	12.50(0.35)	5.22(2.14)	0.73	9.98(2.04)	8.86(1.58)
89	G178.72-07.01	178.725/-7.012	4.96(0.27)	4.53(2.64)	0.80	2.20(2.14)	3.12(3.00)
90	G178.98-06.74	178.989/-6.749	11.00(0.43)	1.93(0.96)	0.80	8.45(2.56)	6.68(1.73)
91	G181.42-03.73	181.428/-3.733	4.09(0.61)	2.28(0.86)	0.90	...	3.16(0.67)
92	G181.84+00.31	181.846/0.317	3.11(0.73)	0.37(0.12)	0.90	...	3.58(1.39)
92	G181.84+00.31	181.846/0.317	8.79(0.74)	1.46(0.74)	0.90	...	3.58(1.39)
95	G192.28-11.33	192.283/-11.339	13.20(0.54)	4.91(1.78)	0.60	0.82(0.66)	1.48(1.13)
100	G046.75-07.68	46.76/-7.69	4.15(0.43)	1.96(1.07)	0.67	...	0.65(0.32)
102	G048.25-05.73	48.25/-5.74	7.38(0.36)	4.09(1.91)	0.66	...	3.97(1.25)
112	G054.03-02.38	54.03/-2.39	6.79(0.57)	1.89(0.97)	0.74	...	1.24(0.29)
113	G056.84+04.81	56.84/4.82	6.76(0.64)	7.00(3.32)	0.63	...	1.10(0.37)
115	G057.10+03.65	57.11/3.66	19.90(0.71)	2.67(1.25)	0.72	...	5.67(1.17)
118	G058.02+03.02	58.03/3.02	9.27(0.50)	5.29(3.67)	0.80	...	2.87(0.94)
119	G058.07+03.20	58.07/3.21	12.50(0.59)	1.37(0.65)	0.78	...	2.23(1.08)
122	G060.75-01.23	60.75/-1.23	12.10(0.87)	0.90(0.43)	0.91	0.71(0.58)	2.79(1.49)
126	G070.72-00.63	70.73/-0.63	10.40(1.20)	1.30(0.57)	0.76	...	13.70(7.08)
127	G037.49+03.03	37.49/3.03	9.92(0.53)	4.73(2.68)	0.72	...	1.48(0.70)
132	SDC033.107-0.065	33.107/-0.065	37.20(5.36)	0.22(0.08)	0.98	...	1.07(0.26)
136	SDC033.622-0.032	33.622/-0.032	42.20(2.49)	0.44(0.18)	0.98	...	1.90(0.13)
138	SDC033.743-0.009	33.743/-0.009	36.40(2.49)	1.10(0.35)	0.98	...	0.91(0.33)
139	SDC033.819-0.217	33.819/-0.217	33.50(2.79)	0.79(0.44)	0.97	...	4.33(0.52)
141	SDC034.685-0.729	34.685/-0.729	18.30(1.59)	0.59(0.30)	0.96	...	3.85(0.21)